International Journal of Coal Geology 191 (2018) 135–151

Contents lists available at ScienceDirect

International Journal of Coal Geology

journal homepage: www.elsevier.com/locate/coal

Assessing low-maturity organic matter in shales using Raman spectroscopy: Effects of sample preparation and operating procedure

Delano G. Henry[a,*], Ian Jarvis[a], Gavin Gillmore[a], Michael Stephenson[b], Joseph F. Emmings[c]

[a] Department of Geography and Geology, Kingston University London, Kingston upon Thames KT1 2EE, UK
[b] British Geological Survey, Keyworth, Nottingham NG12 5GG, UK
[c] School of Geography, Geology and the Environment, University of Leicester, Leicester LE1 7RH, UK

ARTICLE INFO

Keywords:
Raman spectroscopy
Organic matter
Kerogen
Maturity
Shale
Automated spectral analysis

ABSTRACT

Laser Raman spectroscopy is used to assess the thermal maturity of organic matter in sedimentary rocks, particularly organic-rich mudstones. However, discrepancies exist between quantified Raman spectral parameters and maturity values obtained by vitrinite reflectance. This has prevented the adoption of a standard protocol for the determination of thermal maturity of organic matter (OM) by Raman spectroscopy. We have examined the factors influencing the Raman spectra obtained from low-maturity OM in potential shale gas reservoir rocks. The inconsistencies in Raman results obtained are due to three main factors that are critically evaluated: (1) different operational procedures, including experiment setup and spectral processing methods; (2) different methods of sample preparation; (3) the analysis of diverse types of OM. These factors are scrutinized to determine the sources of inconsistency and potential bias in Raman results, and guidance is offered on the development of robust and reproducible analytical protocols. We present two new Raman parameters for un-deconvolved spectra named the DA1/GA ratio (area ratio of 1100–1400 cm^{-1}/1550–1650 cm^{-1}) and SSA (scaled spectrum area: sum of total area between 1100 and 1700 cm^{-1}) that offer potential maturity proxies. An automated spreadsheet procedure is presented that processes raw Raman spectra and calculates several of the most commonly used Raman parameters, including the two new variables.

1. Introduction

Laser Raman spectroscopy is being increasingly used to assess the thermal maturity of organic matter (OM) in sedimentary rocks (Pasteris and Wopenka, 1991; Spötl et al., 1998; Kelemen and Fang, 2001; Beyssac et al., 2002; JehličKa et al., 2003; Marshall et al., 2005; Quirico et al., 2005; Rahl et al., 2005; Schopf et al., 2005; Zeng and Wu, 2007; Aoya et al., 2010; Guedes et al., 2010; Muirhead et al., 2012, 2016; Liu et al., 2013; Kouketsu et al., 2014; Mcneil et al., 2015; Bonoldi et al., 2016; Deldicque et al., 2016; Ferralis et al., 2016; Lünsdorf, 2016; Lünsdorf et al., 2017; Lupoi et al., 2017; Sauerer et al., 2017; Schito et al., 2017). The novelty of Raman spectroscopy is that it is a non-destructive method that allows for rapid data acquisition with fast and easy interpretation, combining both optical microscopy and vibrational spectroscopy. Laser Raman has the ability to be used alongside other petrological parameters in order to reduce risk, as well as being applied where other maturity indicators such as vitrinite reflectance (VR), spore colouration index (SCI), fluorescence spectroscopy and Rock-Eval pyrolysis (T_{max}) fail to provide reliable results. It can also be used as a cheap and rapid means to screen samples before conducting more expensive and time-consuming destructive analyses.

The Raman spectrum of OM consists of two broad bands; the G band (~1600 cm^{-1}), known as the graphite band, and the D band (~1350 cm^{-1}), known as the disordered band (Fig. 1a). Deconvolution can further divide the spectrum into several disordered bands (Fig. 1b; e.g. D1, D2, D3, D4, D5). However, the number of disordered bands that are separated using deconvolution is controversial, and authors have used a combination of different bands to define laser Raman parameters that can be applied in maturity studies (Spötl et al., 1998; Beyssac et al., 2002; Schopf et al., 2005; Li et al., 2006; Guedes et al., 2010; Lahfid et al., 2010; Liu et al., 2013; Hinrichs et al., 2014; Wilkins et al., 2014; Lünsdorf et al., 2017).

The G band corresponds to an ideal graphitic structure, whereas the D bands are associated with chemical and structural defects in the crystal lattice. As temperature increases, the chemical defects are expelled from the crystal lattice and the remaining carbon undergoes reorganization into a more ordered carbon structure, until it reaches the metamorphism stage where the carbon residue transforms into perfectly ordered graphite (Buseck and Beyssac, 2014). Laser Raman analyses the chemical structure of OM, and in theory, should be able to

* Corresponding author.
E-mail address: k1119111@kingston.ac.uk (D.G. Henry).

https://doi.org/10.1016/j.coal.2018.03.005
Received 7 February 2018; Received in revised form 14 March 2018; Accepted 15 March 2018
Available online 17 March 2018

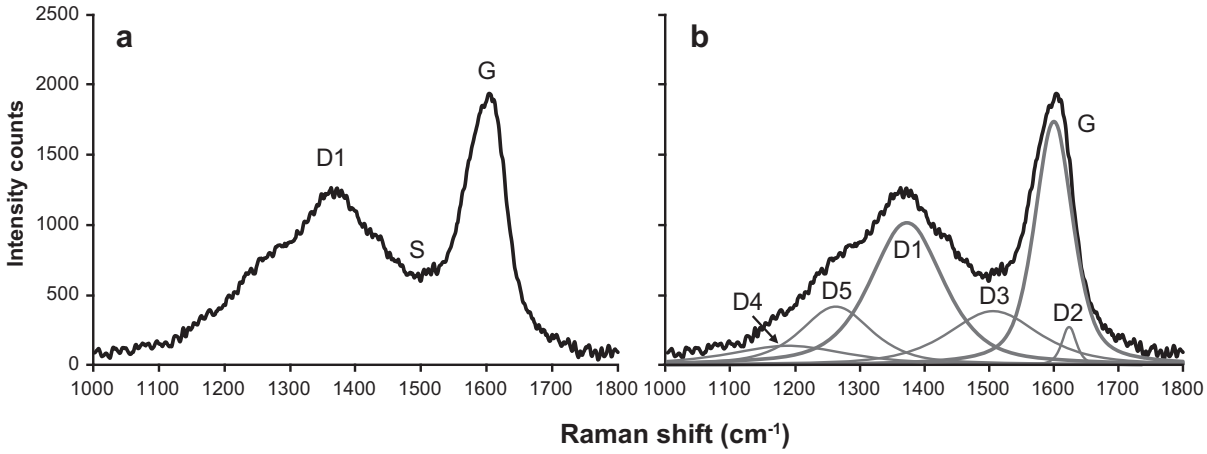

Fig. 1. Raman spectral characteristics. (a) Un-deconvolved organic matter spectrum (b) Common six band deconvolution outcome for an organic matter spectrum. D = disordered bands (1, 2, 3, 4, 5); G = graphitic band; S = saddle.

track the thermal evolution of OM. The current study aims to assess the application of laser Raman to characterise OM maturity in the lower temperature oil- and gas-generation stages of catagenesis (50 – 150 °C). An improved analytical method has great potential to be used in the evaluation of shale gas plays, as well as being applied to the wider analysis of petroleum basins.

Some of the most commonly used parameters to track thermal maturity are summarized in Table 1, which include the heights, widths, areas and positions of the disordered and graphitic (ordered) bands. It should be noted that there is some ambiguity with the terms RA1 and RA2: Chen et al. (2017) used different equations to calculate these parameters compared to variables of the same name reported previously by Lahfid et al. (2010).

Inconsistent quantified Raman parameter and maturity values obtained by VR are apparent in the literature (Kelemen and Fang, 2001; Quirico et al., 2005; Guedes et al., 2010; Lahfid et al., 2010; Liu et al., 2013; Wilkins et al., 2014). In this study three factors are examined as likely sources for this inconsistency: (1) different operational procedures employed, including experiment setup and spectral processing methods; (2) different methods of sample preparation; (3) analysis of diverse types of OM, and intra-particle variability. These three factors have also been discussed by Lünsdorf et al. (2014).

(1) Operational procedures may be divided into two categories: (a) experimental setup; (b) spectral processing methods.
   (a) The laser wavelength, laser power, accumulation time and number of accumulations employed by different authors are highly variable (Appendix 1). Here, we will assess the optimum

Table 1
Raman parameters used to determine the maturity of organic material, along with the abbreviations used in previous studies.[a]

Method	Parameters	Abbreviations	References
Full width at half maximum of a band (FWHM)	G	G-FWHM	Hinrichs et al. (2014); Zhou et al. (2014); Schmidt et al. (2017); This study.
	D1	D-FWHM	Quirico et al. (2005); Bonoldi et al. (2016); Schito et al. (2017); This study.
	D1/G		Spötl et al. (1998); JehličKa et al. (2003).
Ratio of Raman band height intensity	D1/G	R1	Rahl et al. (2005); Schmidt et al. (2017); Sauerer et al. (2017); Roberts et al. (1995); Spötl et al. (1998); Kelemen and Fang (2001); This study.
	G/S	Saddle Index	Wilkins et al. (2014); This study.
Ratio of band areas	D/G	RA1[b]	Chen et al. (2017).
	D1/(G + D1 + D2)	R2	Rahl et al. (2005); Chen et al. (2017).
	S2/(S1 + S2)	R3	Beyssac et al. (2002).
	(D1 + D4)/(D1 + D2 + D3 + D4 + G)	RA1[b]	Lahfid et al. (2010).
	(D1 + D4)/(D2 + D3 + G)	RA2[b]	Lahfid et al. (2010).
	D2/G	RA2[b]	Chen et al. (2017).
	D3/G	RA3	Chen et al. (2017).
	D4/G	RA4	Chen et al. (2017).
	G/(D1 + D2 + D3 + D4 + G)	RA5	Chen et al. (2017).
Area of Raman spectra regions	$Area_{(1100–1400)}/Area_{(1550–1650)}$	DA1/GA	This study.
	$Area_{(1100-1300)}/Area_{(1300–1370)}$	RIP (Raman Index of Preservation)	Schopf et al. (2005); Du et al. (2014); This study.
Raman band position	G–D1	RBS (Raman Band Separation)	Mumm and İnan (2016); Sauerer et al. (2017); Schmidt et al. (2017); Schito et al. (2017); This study.
	G	–	Spötl et al. (1998); Du et al. (2014); İnan et al. (2016).
	D1	–	Spötl et al. (1998); Chen et al. (2017).
Scaled spectrum area	$Area_{(1100–1700)}$	SSA	This study.
Scaled total area	Sum of scaled individual bands after deconvolution	STA	Lünsdorf (2016); Lünsdorf et al. (2017)

[a] Refer to Fig. 1 for G, D, S and D1–D4 band positions.
[b] It should be noted that there is some ambiguity with the terms RA1 and RA2: Chen et al. (2017) used different equations to calculate these parameters compared to variables of the same name reported previously by Lahfid et al. (2010).

experimental setup that considers the speed of analysis, damage to the sample, and the signal to noise ratio.

(b) Typically, processing the Raman spectra include smoothing, a linear or non-linear baseline correction, followed by deconvolution of two (Hinrichs et al., 2014; Wilkins et al., 2014; Schmidt et al., 2017), three (Court et al., 2007), four (Beyssac et al., 2002; Rahl et al., 2005; Aoya et al., 2010), five (Lahfid et al., 2010; Chen et al., 2017; Sauerer et al., 2017), or six or more bands (Schopf et al., 2005; Li et al., 2006; Guedes et al., 2010; Bonoldi et al., 2016; Ferralis et al., 2016; Schito et al., 2017) (Appendix 1). Deconvolution enables the operator to assess a suite of Raman parameters (Table 1) for individual bands. Several common deconvolution methods will be tested against the automated method developed in this study, which does not perform deconvolution, in order to acquire Raman parameters. The method and Raman parameters will be compared.

(2) A comparison of different sample types from several rock samples will be assessed to determine if there is a difference in Raman spectral parameters. Previous studies have analysed polished blocks of isolated OM (Pasteris and Wopenka, 1991; Beyssac et al., 2003; Nestler et al., 2003; Rahl et al., 2005; Allwood et al., 2006; Marques et al., 2009; Guedes et al., 2010; Kwiecinska et al., 2010; Mathew et al., 2013; Hinrichs et al., 2014; Kouketsu et al., 2014; Wilkins et al., 2014; Mumm and İnan, 2016), as well as strew-mounted slides (Roberts et al., 1995; Spötl et al., 1998; Rantitsch et al., 2004; Lünsdorf et al., 2014), and rock chips (Muirhead et al., 2016; Sauerer et al., 2017). Some authors demonstrated that polishing OM impacts the Raman spectrum (Beyssac et al., 2003; Ammar and Rouzaud, 2012; Lünsdorf, 2016). This is examined further here.

(3) Different maceral types may behave differently under different thermal conditions as demonstrated by the Van Krevelen diagram (Tissot et al., 1974), so ensuring that the same maceral type is analysed throughout a geological section is generally essential. The effect of maceral type on Raman parameters is assessed here, together with an examination of intra-particle variability.

2. Materials and methods

2.1. Materials

The Late Mississippian (Namurian) Bowland Shale is the main target for shale gas exploration in the UK, with an estimated 1329 trillion cubic feet of hydrocarbons in-place (Andrews, 2013; Stephenson, 2014; Delebarre et al., 2017). The shales were deposited in NE-SW epicontinental seaways between Gondwana and Laurussia. A phase of back-arc extension north of the Variscan orogenic front formed a series of interconnected graben and half-graben structures (Waters et al., 2009, Fig. 2). These basins accumulated Carboniferous organic-rich mudstones, which have been identified as a proven source rocks for many of the conventional oil and gas fields in the UK Midlands (DECC, 2010).

Four Mississippian (Arnsbergian; early Serpukhovian) Morridge Formation (equivalent to the Bowland Shale; Waters et al., 2009) core samples from the Carsington Dam Reconstruction C4 borehole (53.04898°N 1.63790°W, Derbyshire, England) in the Widmerpool Gulf were analysed (Fig. 2). Raman analyses were performed on polished blocks of isolated OM and strew slides. These samples are in the early oil window (Könitzer et al., 2014, 2016; Hennissen et al., 2017) and came with comprehensive palynofacies and geochemical data (Table 2). T_{max} values range between 424 and 440 °C (Könitzer et al., 2016), and the calculated $\%_{eq}VR_o$ using T_{max} values (cf. Jarvie et al., 2001; Eq. (1)) range from 0.5–0.8$\%_{eq}VR_o$, indicating immature to early maturity.

$$\text{Calculated}\%_{eq}VR_o = (0.0180 \times T_{max}) - 7.16 \quad (1)$$

This agrees with the vitrinite reflectance values of < 0.6$\%VR_o$ obtained by Smith et al. (2010) from the area. Production Index (PI) values determined from Rock-Eval data by Könitzer et al. (2016) range from 0.06 to 0.09, straddling between immature and the oil generation window.

Two outcrop samples of the Upper Bowland Shale (Pendleian; early Serpukhovian) from a stream section in the Craven Basin (53.97373°N 2.54397°W), Lancashire (Fig. 2; Emmings et al., 2017), were also analysed and compared with the equivalent core material from the Carsington Dam Reconstruction C4 borehole (Table 2). T_{max} values range between 431 and 442 °C, similar to the samples studied by Könitzer et al. (2016), and the calculated VR values using T_{max} range from 0.6–0.8$\%_{eq}VR_o$. However, the PI values range from 0.13–0.26, suggesting that these rocks had reached the oil generation window.

2.2. Methods

2.2.1. Laser Raman

Analyses employed a Renishaw inVia™ laser Raman instrument connected to a Leica DMLM microscope. The Rayleigh scattering was removed using an edge filter and the Raman scattering was dispersed by an 18,000 lines/mm holographic grating and detected by a charged couple device (CCD). A standard silicon wafer sample was used to calibrate the instrument by matching the 520.5 cm^{-1} band position, followed by manually aligning the laser beam with the crosshairs on the microscope. A 514.5 nm argon-ion green laser and a 633 nm HeNe red laser were used. The lasers deliver ~20 mW at 100% power.

The laser was focused through a ×50 objective, with a laser spot size of c. 2 μm. The scan range was limited to 900–2000 cm^{-1}, in order to assess the first-order region. WiRE 3.3 software was used to acquire spectra and perform deconvolution using a pseudo-Voigt function to acquire the band heights, band areas, band positions and full width at half maximum (FWHM) for individual bands (Fig. 1b, cf. Table 1). A Microsoft Excel® spreadsheet was used to process un-deconvolved spectra (Fig. 1a) by performing smoothing operations, baseline corrections and normalization, to acquire the height and position of the saddle height, D1 and G band, G-FWHM, D-FWHM and areas of specific regions using the trapezoid area rule (cf. Table 1; Appendix 2).

2.2.2. Sample preparation

Two different types of sample preparation were performed, both of which used isolated kerogen: (a) polished blocks and (b) strew slides. The kerogen for samples SSK 4522, SSK 4471, HC01–04 and HC02–73 were separated at Kingston University using HCl and HF acid at room temperature to remove the inorganic mineral fraction. Samples were first washed with tap water, air-dried and crushed to millimetre-sized fragments. The crushed material was treated with 100 mL of 12 M HCl for 24 h, followed by 100 mL of 23 M HF for several days at room temperature, in order to digest carbonates and silicates, respectively. After each acid treatment, the concentrated solution was diluted with 900 mL of deionized water and then sieved through a 15-μm polyester mesh. Deionized water was used to rinse the sample through the sieve until pH neutral. Following the final rinse, samples were stored in 50 mL glass vials with deionized water. Samples MPA 61616 and MPA 61619 were prepared at the British Geological Survey using a similar technique and a 10-μm sieve (Könitzer et al., 2016).

The strew slides were prepared by spreading c. 0.5 mL of fluid mixture (composed of OM and deionized water) onto a glass slide using a pipette, which was then left to air dry. Polished blocks were constructed by embedding isolated kerogen with epoxy resin in 2.5 cm diameter moulds, followed by grinding using P400, P600, P800, P1200, P2500 silicon carbide paper using water as a lubricant. The samples were then polished using a diamond liquid suspension of 9 μm, 6 μm, 3 μm, 1 μm and were finished off with a 0.04 μm colloidal silica suspension. This grinding and polishing procedure follows the BS ISO 7404-2:2009 standard.

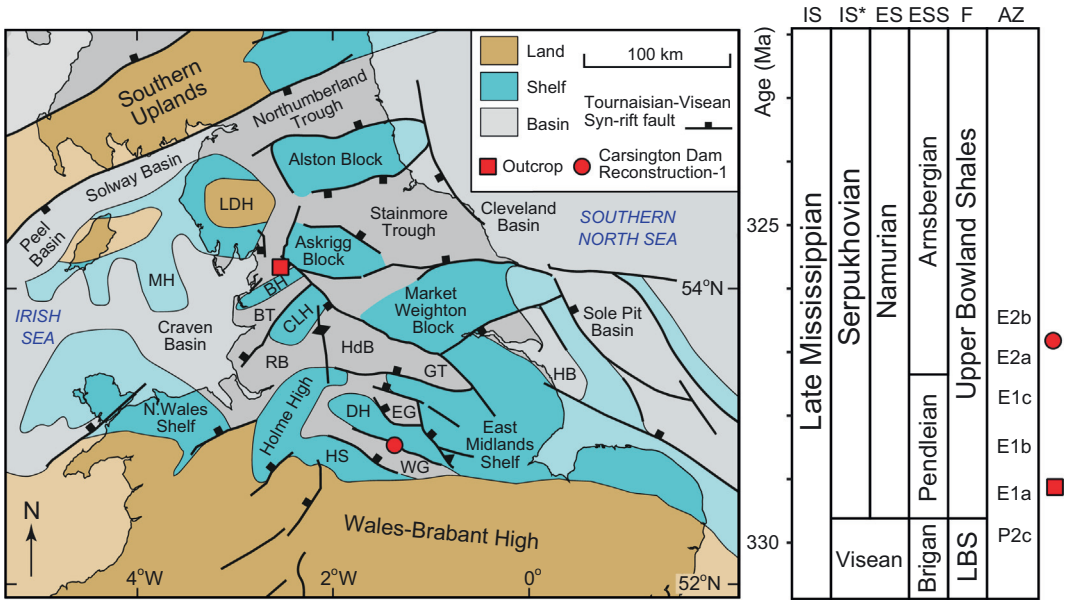

Fig. 2. Tectonic framework of the Mississippian for northern England and Wales showing the location and stratigraphic ages of the samples used in this study. IS – International series; IS* – international stage; ES – European stage; ESS – European substage; F – Formation; AZ – ammonoid zones; Brigan – Brigantian; LBS – Lower Bowland Shales. Tectonic units: BH – Bowland High; BT– Bowland Trough; CLH– Central Lancashire High; DH – Derbyshire High; EG – Edale Gulf; GT – Gainsborough Trough; Hdb – Huddersfield Basin; HB – Humber Basin; HS – Hathern Shelf; LDH – Lake District High; MH – Manx High; RB – Rossendale Basin; WG– Widmerpool Gulf. Base map from Waters et al. (2009). Reproduced with the permission of the British Geological Survey ©NERC. All rights reserved.

2.2.3. Organic matter classification

Strew slides were used to investigate whether different types of OM influence the Raman parameters. The OM categories identified in transmitted white light (Appendix 3), following Tyson (1995) were:

(1) Translucent phytoclast (Fig. A3.1): Translucent particles under transmitted light with colours ranging from light brown to dark brown, typically equant or lath-shaped with angular margins. The phytoclasts can be striate, striped, banded or pitted. Particles that appear opaque but have brown rims or brown patches are also included in this group.
(2) Opaque phytoclast (Fig. A3.2): The particles appear fully opaque under transmitted light. The shape of the particles varies from equant, lath or rounded, and the margins can be angular or corroded. They often have no internal structure, however, lath-shaped particles may be pitted. These particles are equivalent to inertinite when examining polished blocks under reflected light; they are the product of either intense oxidation or forest fires (Tyson, 1995).
(3) Pseudo-amorphous phytoclast (Fig. A3.3): These amorphous particles exhibit a patchy, spotted appearance and are light brown to dark brown/black. Most of the biostructure has been lost and the edges are typically diffuse. However, some particle edges are sharp and straight, suggesting a remnant border of a degraded phytoclast.
(4) AOM (Fig. A3.4): The amorphous OM (AOM) is a structureless heterogeneous to homogenous particle with irregular diffuse margins under transmitted light. Colour typically ranges from pale yellow-brown to greyish. AOM may represent bacterial and/or reworked/degraded algal OM (Tyson, 1995). Pyrite is often present as inclusions. Fluorescence microscopy was not used in this study, so further subdivision of the AOM group was not possible. Consequently, all AOM particles were grouped together.

2.2.4. Experimental methodology

2.2.4.1. Testing different operational procedures. Different operational procedures were tested on strew slides. First, the experimental setup was tested by comparing results from a 514.5 nm argon-ion green laser and a 633 nm HeNe red laser, followed by an analysis of how different accumulation times, number of accumulations, and laser powers affect the spectra. Spectral processing was assessed by comparing smoothing vs. non-smoothing, linear vs. 3rd-order polynomial baseline corrections, and deconvolution vs. the automated non-deconvolution method developed in this study to determine Raman parameters.

2.2.4.2. Testing different samples types. The Raman characteristics of polished blocks and strew slides were tested using the optimum operational settings and procedures developed above: 514.5 nm

Table 2
Samples studied from the Carsington Dam Reconstruction C4 borehole (CD) and outcrop section.

Type	Sample name	Lithology	Summary of palynology	Rock-Eval parameters[a]					
				TOC (%)	T_{max} (°C)	HI	OI	PI	$\%_{eq}VR_o$
CD	SSK 4522	Calcareous mudstone	90% AOM; 10% terrestrial	1.8	425	330	17	0.06	0.49
	SSK 4471	Siltstone	20% AOM; 80% terrestrial	nd	nd	nd	nd	nd	nd
	MPA 61616	Silt-bearing mudstone	30% AOM; 70% terrestrial	1.1	440	96	29	0.09	0.76
	MPA 61619	Calcareous mudstone	90% AOM; 10% terrestrial	nd	nd	nd	nd	nd	nd
Outcrop	HC01-04	Mudstone	90% AOM; 10% terrestrial	3.87	432	141	0	0.18	0.62
	HC02-73	Mudstone	80% AOM; 20% terrestrial	2.19	431	163	1	0.26	0.60

[a] TOC = total organic carbon, HI = hydrogen index, OI = oxygen index, PI = production index. $\%_{eq}VR_o$ calculated using Jarvie et al. (2001) equation (Eq. (1)). AOM = amorphous organic matter, nd = not determined. CD data from Könitzer et al. (2016), outcrop data from Emmings et al. (2017).

argon-ion green laser wavelength, 10 s accumulation time, 2 accumulations and a 0.2 mW laser power, this was kept constant throughout. Following acquisition, a Microsoft Excel® worksheet (Appendix 2) processes and determines the Raman parameters by performing a Savitzky-Golay smoothing filter using a 21-point quadratic polynomial algorithm, a linear or a 3rd-order polynomial baseline correction, followed by normalization at the same maximum G height intensity of 2000 counts, as well as automatically calculating the R1, RBS, G-FWHM, D-FWHM, RIP, DA1/GA and STA Raman parameters. Deconvolution was not performed. Comparisons between the different sample types were made by: (1) visual comparison of the spectra; and (2) comparing the Raman parameters.

2.2.4.3. Testing different organic matter types. Different types of OM were assessed using strew slides in transmitted light. This experiment was performed under the optimum instrument conditions. Spectra processing and calculation of the Raman parameters were performed using the Microsoft Excel® automated worksheet (Appendix 2). Deconvolution was not performed.

3. Results

3.1. Experimental setup

Fig. 3 shows a comparison of the spectra obtained from a phytoclast in a strew slide using laser wavelengths of 514.5 (argon ion) and 633 nm (HeNe). The 514 nm laser wavelength produces a significantly better quality spectrum that has a smoother more linear baseline, and better peak-to-background ratios, as observed previously by Quirico et al. (2005).

When using a laser power of 1 mW or greater, the laser damages the surface of the OM (Fig. 4). Evidence of in-situ burning caused by the laser was observed as a small black spot (Fig. 4c, d). In-situ burning also influences the Raman spectrum (Fig. 4f). The position of the G band blue-shifts, as described by Allwood et al. (2006), and the saddle height and the D band also increases in height with respect to the G band. Consequently, laser powers > 0.2 mW are not advised as they alter the Raman spectrum.

Spectra acquired using a 0.02 mW and 0.2 mW laser power are consistent; therefore, the 0.2 mW laser power does not damage or alter the OM. Fig. 5 demonstrates that using a 0.2 mW laser power improves the signal to noise ratio compared to using a 0.02 mW laser power. Increasing the accumulation time and number of accumulations also slightly increases the signal to noise ratio, particularly when using a lower laser power of 0.02 mW (compare Fig. 5a–d).

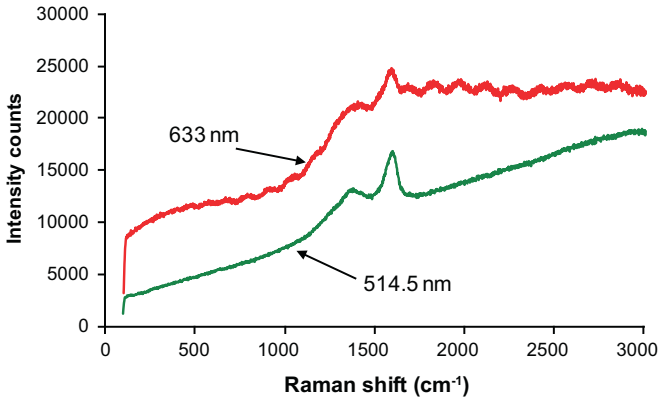

Fig. 3. Comparison of the Raman spectra acquired for a translucent phytoclast in a strew slide from sample SSK 4471 using a 633 nm (red) and 514.5 nm (green) laser. The 633 nm laser produces more fluorescence than the 514.5 nm wavelength. (For interpretation of the references to colour in this figure legend, the reader is referred to the web version of this article.)

3.2. Processing the spectra

3.2.1. Smoothing

Performing a smoothing procedure removes noise from the spectrum, allowing the operator to pick band heights and positions with less ambiguity. Smoothing the spectrum also reduces uncertainty during baseline correction, as the noise in the spectrum can greatly influence the heights of individual control points, leading to anomalous baseline corrections (Fig. 6). This can be a major problem especially if control points are fixed when performing an automated procedure. After smoothing, noise is drastically reduced and the control points are less prone to sharp random increases in height, which makes the baseline corrections more reproducible (Fig. 6).

Deconvolution also becomes more reproducible after smoothing, as noise can impact the fitted bands. Fig. 7 shows that when smoothing is performed, the fitted spectrum has a better fit with the original spectrum. The height and widths for the D3, D4 and D5 fitted bands for an un-smoothed and smoothed spectrum are significantly different, even though the starting spectrum is the same. Raman parameters may also differ substantially (Fig. 8).

3.2.2. Baseline correction

Fluorescence is a common problem in low-maturity OM that can alter the Raman spectra and parameters. Therefore, an unbiased baseline correction method needs to be adopted. Here, two of the most commonly used baseline corrections were tested: (1) linear; and (2) 3rd-order polynomial. Each acquired spectrum has a wavenumber range from 900 to 2000 cm^{-1} to better estimate the shape of the background fluorescence, and a smoothing procedure was performed before the baseline was corrected. The control points for the linear function were fixed at 1000 cm^{-1} and 1800 cm^{-1}, and for the 3rd-order polynomial function the control points are 2000 cm^{-1}, c.1850 cm^{-1}, c.1050 cm^{-1} and 900 cm^{-1}. The positions of the control points were chosen, on the basis that they lie outside the spectral range influenced by OM. The position of the control points at c.1850 cm^{-1} and c.1050 cm^{-1} for the 3rd-order polynomial correction may be shifted ± 20 cm^{-1}, if the baseline correction does not fit the background shape. An automated worksheet in Microsoft Excel® was developed to perform these tasks (Appendix 2).

When fluorescence is present, which is often the case for low-maturity OM, a 3rd-order polynomial baseline correction works best (Fig. 9). A linear baseline correction performed on samples that experience non-linear fluorescence will result in the D band and saddle height to increase in height in relation to the G band, which will lead to an increase in the R1 ratio, RIP, and SSA Raman parameters, and a decrease in the saddle index (Fig. 9). Fig. 10 shows 20 overlain spectra that have had a linear and a 3rd-order polynomial baseline correction acquired from the same strew slide. Notice the larger scatter for the linear baseline correction, compared to the 3rd-order polynomial baseline correction.

3.2.3. Calculating Raman parameters

Five methods to derive Raman parameters were assessed (Table 3). Deconvolution was not performed for the M-1 and M-2 methods, but is employed in the M-3, M-4 and M-5 methods (Fig. 11). Deconvolution was performed using Renishaw's WiRE 3.3™ software on a smoothed, 3rd-order polynomial baseline corrected, normalized spectra with a tolerance of 0.01 and a maximum of 15 iterations. The descriptions in Table 3 should be followed precisely, as the initial attributes (height, width, position) of the curves before fitting can significantly alter the parameters. The closeness of fit of the fitted spectrum to the original spectrum after deconvolution may be assessed by: (1) visually comparing the original and fitted spectrum; (2) root-mean-square error (RMSE); and (3) the coefficient of determination (R^2). The D2 band was not included in any of the deconvolution methods, as it cannot be identified in low-maturity samples, as observed also by Beyssac et al.

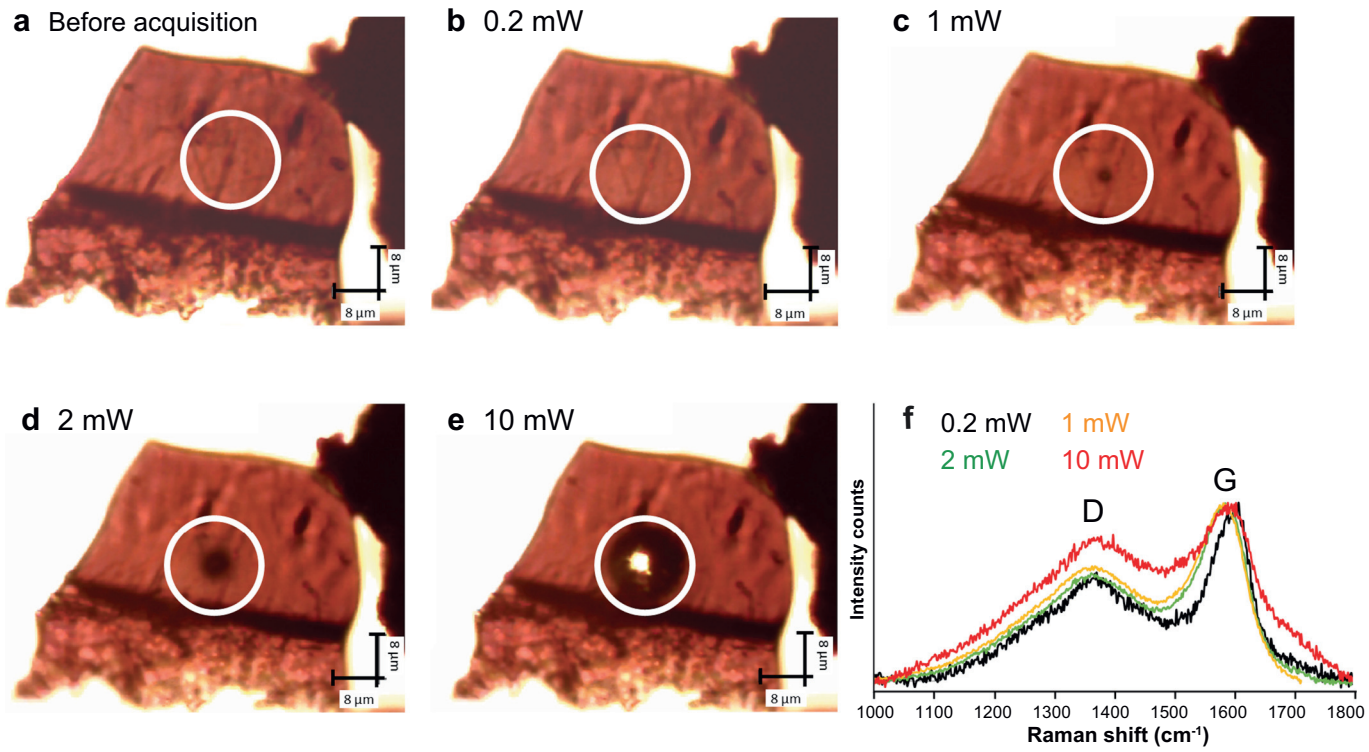

Fig. 4. Images before and after spectra acquisition of a phytoclast from a strew slide (SSK 4471) using a laser wavelength 514 nm, with associated Raman spectra. The white circles highlight the area where the measurements were taken. Scale bar is 8 µm. (a) before spectra acquisition. Image after spectra acquisition using: (b) 0.2 mW; (c) 1 mW; (d) 2 mW; (e) 10 mW laser power. (f) associated spectra using the different laser powers.

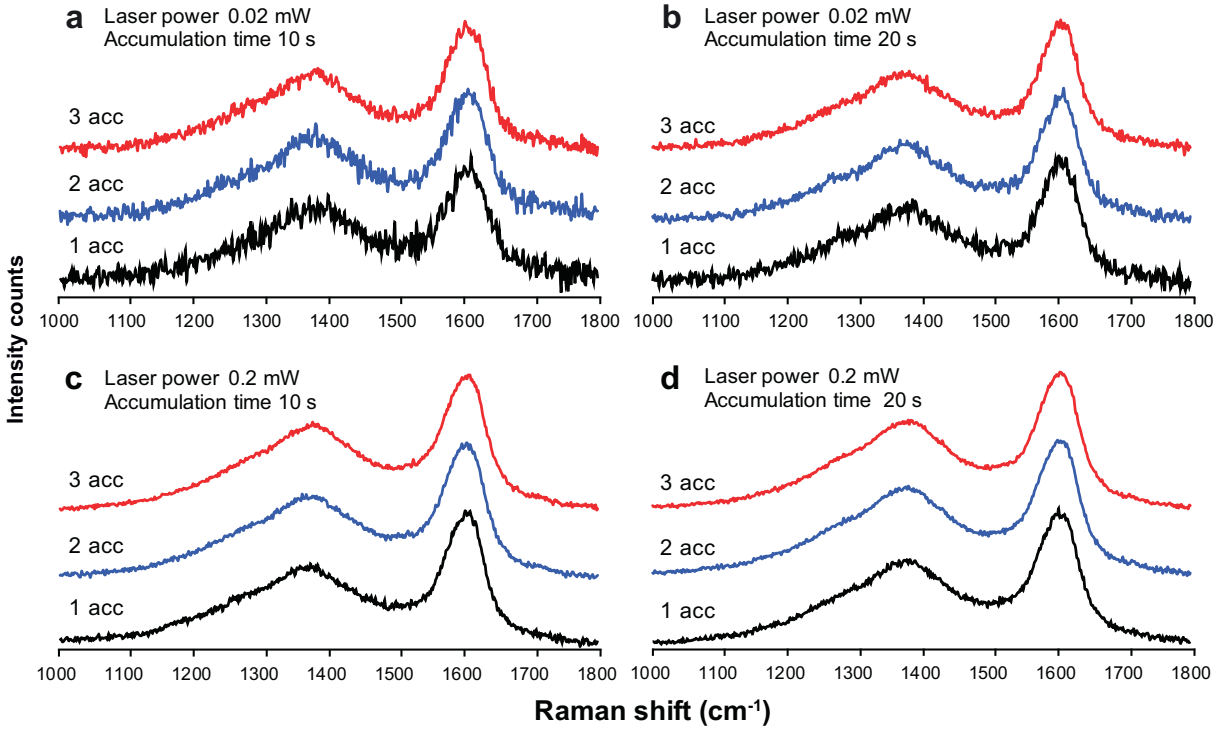

Fig. 5. Comparison of the spectra acquired from the same spot using variable laser power, accumulation time and number of accumulations. (a) 0.02 mW laser power with a 10 s accumulation time, with 1–3 accumulations. (b) 0.02 mW laser power with a 20 s accumulation time. (c) 0.2 mW laser power with a 10 s accumulation time. (d) 0.2 mW laser power with a 20 s accumulation time. Note that the 0.2 mW laser produces a significantly better signal to noise ratio than using the 0.02 mW laser power, and shows no significant improvement for a signal accumulation time > 10 s.

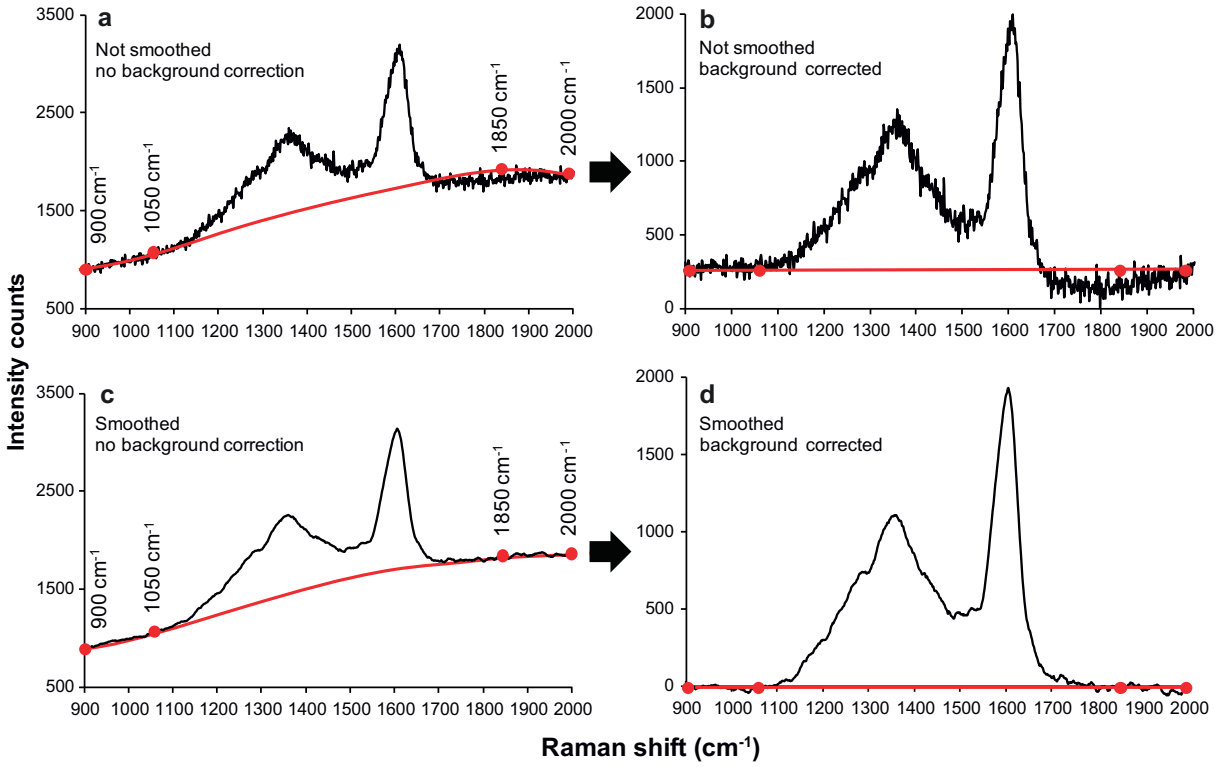

Fig. 6. An example of how noise can affect an automated background correction; a–d are all the same original spectra from a translucent phytoclast (sample SSK 4471). (a) An unsmoothed spectrum with the predicted background shape. (b) Outcome of the background correction from spectra (a). (c) A smoothed spectrum with the predicted background shape. (d) Outcome of the background correction (c). Note the sharp peaks created by the noise in (a) affects the control point at 1850 cm^{-1}; here the control point lies above the trend of the background and the resulting spectrum (b) is unsuitable. For a smoothed spectrum the sharp peaks associated with noise are absent and therefore the control points are less affected by noise and produce a better background corrected spectrum.

(2002) and Brolly et al. (2016).

For the M-1 and M-2 methods, the spectra were copied into the automated Microsoft Excel® worksheet, which performs a Savitzky-Golay smoothing filter using a 21-point quadratic polynomial algorithm (Savitzky and Golay, 1964), a 3rd-order polynomial baseline correction, and normalizes the spectra to the same G band height at 2000 counts, followed by calculating the R1, RBS, saddle index, G-FWHM and D-FWHM Raman parameters (See Table 1 and Fig. 11a for how to calculate these parameters). The M-2 method follows the same processing procedures as for M-1, however it also integrates the areas of specific regions using the trapezoid area rule to calculate the RIP (Schopf et al., 2005), DA1/GA and SSA (Tables 1, 3).

For the M-3 method, a two-band deconvolution method was applied for the D1 and G band using a pseudo-Voigt function (Fig. 11), similar to Hinrichs et al. (2014) and Wilkins et al. (2014, 2015). The calculated Raman parameters are R1, RA1, D-FWHM, G-FWHM and RBS (See Table 1 and Fig. 11 for how to calculate these parameters). Visually and statistically the fitted spectrum is a good fit with the original spectrum, however, some bumps on the D1 band limb at ~1250 cm^{-1} are lost. The M-4 method fits four bands, G, D1, D3 and D4, using a pseudo-Voigt function, similar to the Kouketsu et al. (2014) "fitting G" method. The M-5 method fits the G, D1, D3, D4 and D5 bands using a pseudo-Voigt function. Both methods have a good fit with the original spectrum and are statistically better than the M-3 method (Fig. 11).

For the M-5 method, the D3, D4 and D5 bands are highly unstable, and may have unrealistic positions, heights and widths after deconvolution, as illustrated in Fig. 12. The closeness of fit of the fitted spectrum and the original spectrum may be very high for an unsuitable fit where the D3 and D5 bands go rogue. This is also the case for the M-4 method.

The Raman parameters that are compared using the M-1, M-3, M-4 and M-5 methods are the R1 ratio, RBS, G-FWHM and D-FWHM. The R1 and RBS parameter results differ slightly for the different methods (Table 4); the G-FWHM values are lower after performing deconvolution and the D-FWHM values are significantly lower after performing deconvolution. The M-1 method has a lower relative standard deviation (RSD) than the M-3, M-4 and M-5 methods, with some exceptions.

The outcrop samples (HC01-04 and HC02-73) have higher RBS and lower G-FWHM values for all the methods, suggesting that they are slightly more mature (Guedes et al., 2010; Liu et al., 2013). This is consistent with the PI (production index) data (Emmings et al., 2017), which also implies increased maturity compared to the Carsington Dam Reconstruction C4 borehole samples.

Overall, performing deconvolution slows down Raman spectra analysis and the individual Raman bands can vary significantly, making visual checks essential. This is not the case when performing the M-1 or M-2 methods, which do not involve deconvolution. Therefore, the M-1 and M-2 methods will be utilized in the subsequent sections.

3.3. Sample types

Raman spectra acquired from a polished block and a strew slide from the same sample (Fig. 13), indicate that polishing increases the relative intensity of the D band, the D band position blue-shifts by ~20 cm^{-1}, and the saddle height increases. The G band position remains relatively unaffected by the polishing procedure, however the G-FWHM is affected but not systematically (Fig. 13, Table 5). Table 5 shows that the polishing procedure increases the R1 ratio, in agreement with the results of Ammar and Rouzaud (2012) and Lünsdorf (2016). The R1 ratios from polished blocks also exhibit more scatter and have a random distribution compared to the R1 ratio calculated from strew slides (Fig. 14).

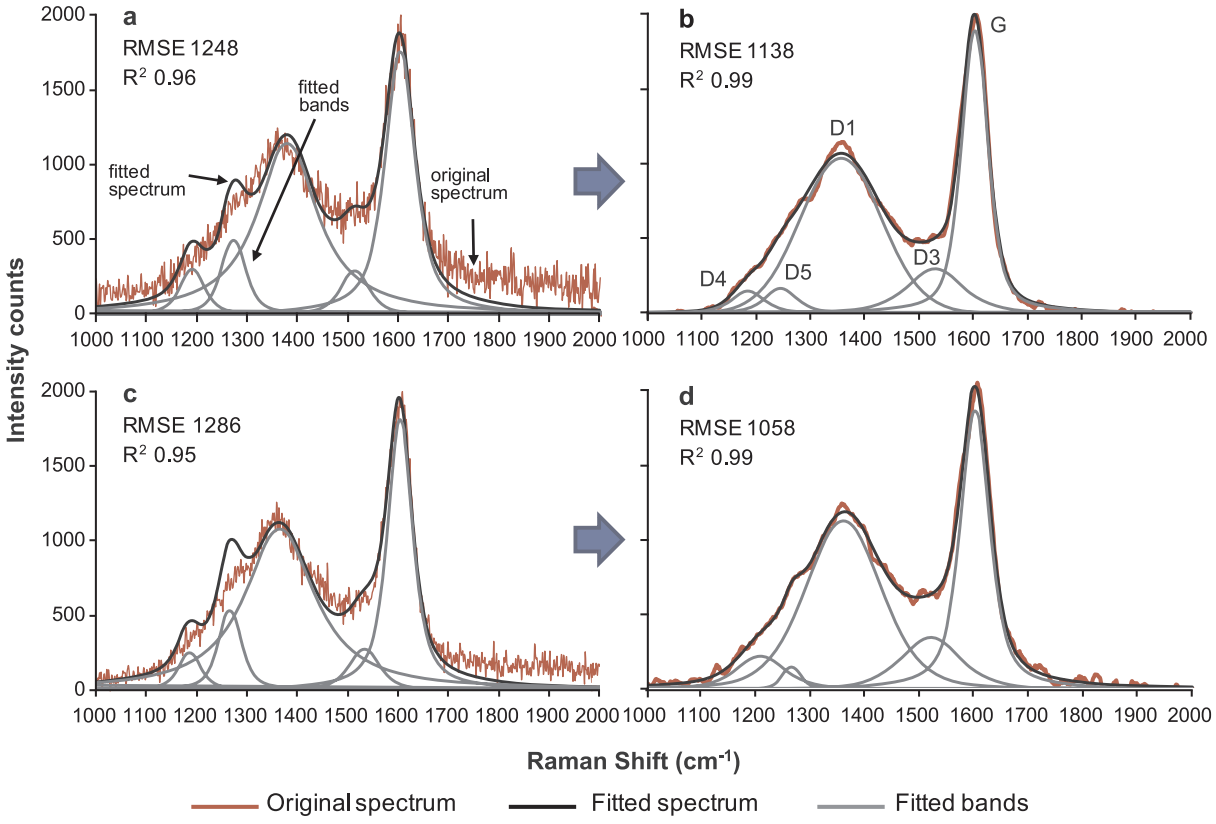

Fig. 7. Different five band deconvolution outcomes when performed on an un-smoothed and smoothed spectrum using the same fitting constraints, from sample SSK 5422. (a) Phytoclast 1 un-smoothed spectra and deconvolution outcome. (b) Phytoclast 1 smoothed spectra and deconvolution outcome. (c) Phytoclast 2 un-smoothed spectra and deconvolution outcome. (d) Phytoclast 2 smoothed spectra and deconvolution outcome. Note that the fitted spectrum for a smoothed spectrum has a better fit with the original spectrum statistically and visually; and that the shape and position of the individual bands are different. RMSE = root-mean-sqaure error.

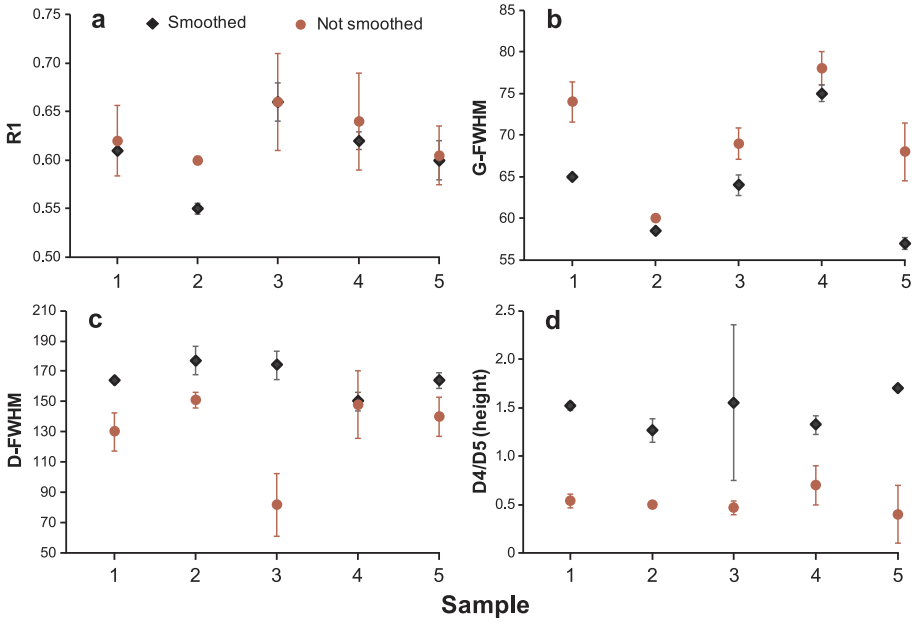

Fig. 8. Raman parameters (Table 1) derived from un-smoothed and smoothed spectra after deconvolution from five translucent phytoclasts in sample HC01-04. (a) R1 ratio. (b) G-FWHM. (c) D-FWHM. (d) D4/D5 band height ratio.

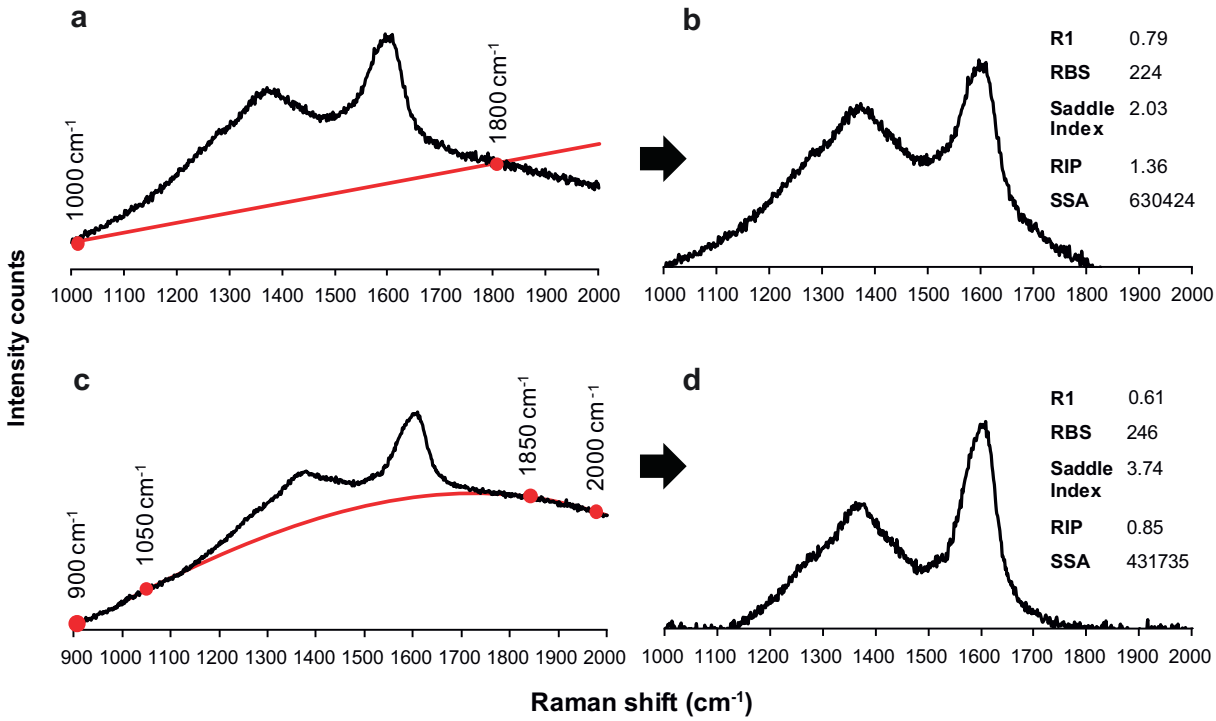

Fig. 9. Comparison of different background corrections on a phytoclast spectrum from sample SSK 4471. (a) Linear baseline correction with the location of the control points. (b) Result of background deconvolution from spectrum (a). (c) 3rd-order polynomial baseline correction with the location of the control points. (d) Result of background correction from spectrum (c). Note the difference in the shape of the spectra and the different Raman parameter values.

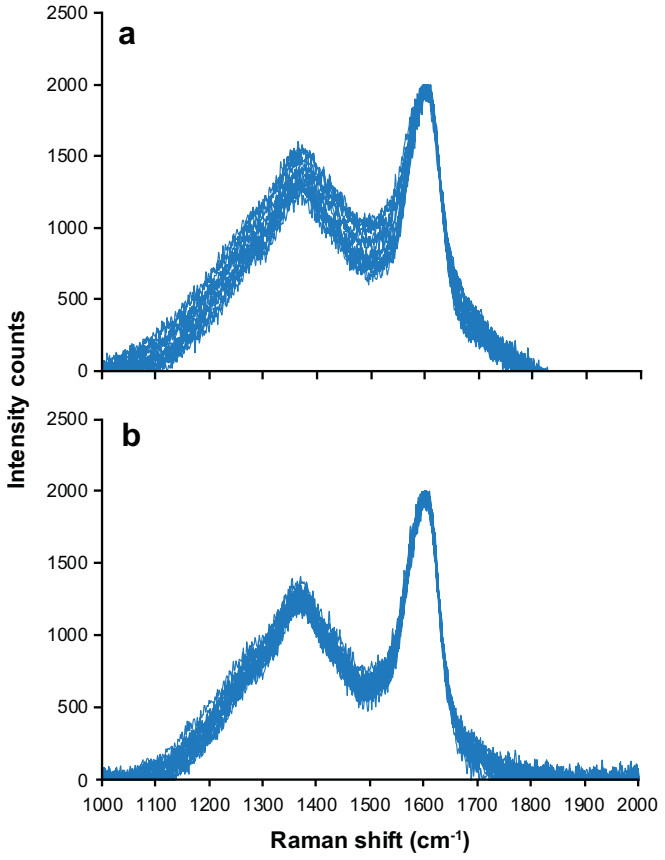

Fig. 10. Twenty AOM spectra from sample HC02-73 overlain after performing (a) linear and (b) 3rd-order polynomial baseline correction. The same original spectra have been used for both methods.

A linear baseline correction performed on polished blocks creates more scatter than 3rd-order polynomial baseline corrections (Table 5). The Raman parameters derived using the latter, lie closer to the strew slide results than for the linear-corrected data. It is clear that the R1 ratio, saddle index, D-FWHM, DA1/GA and SSA are affected by polishing; however, there is no clear evidence that polishing alters the RBS, G-FWHM and RIP values (Table 5). Sample SSK 4471 is an exception, since all the Raman parameters following a 3rd-order polynomial baseline correction become remarkably similar to the strew slide results (Table 5). This will be considered further in the discussion below.

Beyssac et al. (2003) and Kouketsu et al. (2014) reported that polishing effects might be avoided by analyzing immediately below the surface of a particle. Our results do not support this conclusion. Fig. 15 shows the R1 ratio results of a depth profile from an exemplar sample (HC01-04). The mean value derived from a strew slide for the R1 parameter for this sample is 0.61 (horizontal red line in Fig. 15). The R1 values in the depth profiles are substantially greater than the mean value from the strew slide, and despite some scatter, the R1 value does not change systematically with depth.

3.4. Organic matter type and intra-particle variation

The translucent phytoclast group (Fig. A3.1) has similar R1, RIP, D-FWHM, DA1/GA and SSA Raman parameters across the five samples tested (Type 4 in Fig. 16), which is in accordance with all these samples having similar maturities. The G-FWHM, RBS and the saddle index results are more varied across the sample set. The pseudo-amorphous phytoclast (Fig. A3.3) group behaves similarly to the translucent phytoclast group and the Raman parameters are similar (compare Types 3 and 4, Fig. 16). The AOM group (Type 1, Fig. 16; Fig. A3.4) is also similar, with the exception of the R1 and D-FWHM parameters, as the R1 tends to be greater than for other OM types and the D-FWHM is significantly more variable. The opaque phytoclast group (Type 2, Fig. 16; Fig. A3.2) displays the largest variation between OM types, as the parameter values commonly differ substantially from those

Table 3
Methods used to process the spectra and calculate Raman parameters.

Method	Deconvolution	Starting conditions				Description
		Band	cm^{-1}[a]	Height	Width	
M-1	None	na	na	na	na	(1) Smooth spectrum; (2) 3rd-order polynomial baseline correction. The position and heights of the G, D, saddle are recorded to calculate the R1, RBS, saddle index and G-FWHM.
M-2	None	na	na	na	na	(1) Smooth spectrum; (2) 3rd-order polynomial baseline correction; (3) Normalize the spectrum to have a G band intensity of 2000. Use trapezoid area rule to calculate the total area under the curve between 1100–1700 cm^{-1} (SSA); 1100–1400 cm^{-1} (DA1); 1550–650 cm^{-1} (GA). The RIP may also be calculated.
M-3	G, D1	G	1605	2000	40	(1) Smooth spectrum; (2) 3rd-order polynomial baseline correction; (3) Normalize the spectrum to have a G band intensity of 2000; (4) Perform deconvolution using pseudo-Voigt function. Tolerance of 0.01 and maximum of 15 iterations.
		D1	1360	1000	40	
M-4	G, D1, D3, D4	G	1605	2000	40	(1) Smooth spectrum; (2) 3rd-order polynomial baseline correction; (3) Normalize the spectrum to have a G band intensity of 2000; (4) Perform deconvolution using pseudo-Voigt function. Tolerance of 0.01 and maximum of 15 iterations.
		D1	1360	1000	40	
		D3	1500	500	40	
		D4	1240	500	40	
M-5	G, D1, D3, D4, D5	G	1605	2000	40	(1) Smooth spectrum; (2) 3rd-order polynomial baseline correction; (3) Normalize the spectrum to have a G band intensity of 2000; (4) Perform deconvolution using pseudo-Voigt function. Tolerance of 0.01 and maximum of 15 iterations.
		D1	1360	1000	40	
		D3	1500	500	40	
		D4	1160	250	40	
		D5	1260	500	40	

[a] cm^{-1}: centre position of the band. na : not applicable.

obtained for coexisting translucent phytoclasts, pseudo-amorphous phytoclasts and AOM.

Intra-particle OM variation of the Raman parameters vary up to 2–9%RSD. This creates large scatter in the Raman parameter values obtained if only one measurement is taken from an individual particle (Fig. 17). The scatter is reduced to 1–3%RSD, if the average of three measurements from an individual particle is used (Fig. 17). The scatter does not significantly reduce further when performing > 3 measurements.

4. Discussion

This study demonstrates that polished blocks made from isolated OM and strew slides have differing Raman spectra and parameters. Previous authors have noted that polishing OM alters the D band height by inducing disorder in the crystal lattice as the parallel graphene layers "crumple up" (Ammar and Rouzaud, 2012; Lünsdorf, 2016). Our study confirms that R1 Raman parameter values increase after polishing. The R1 ratio from the strew slides have a normal distribution and low range,

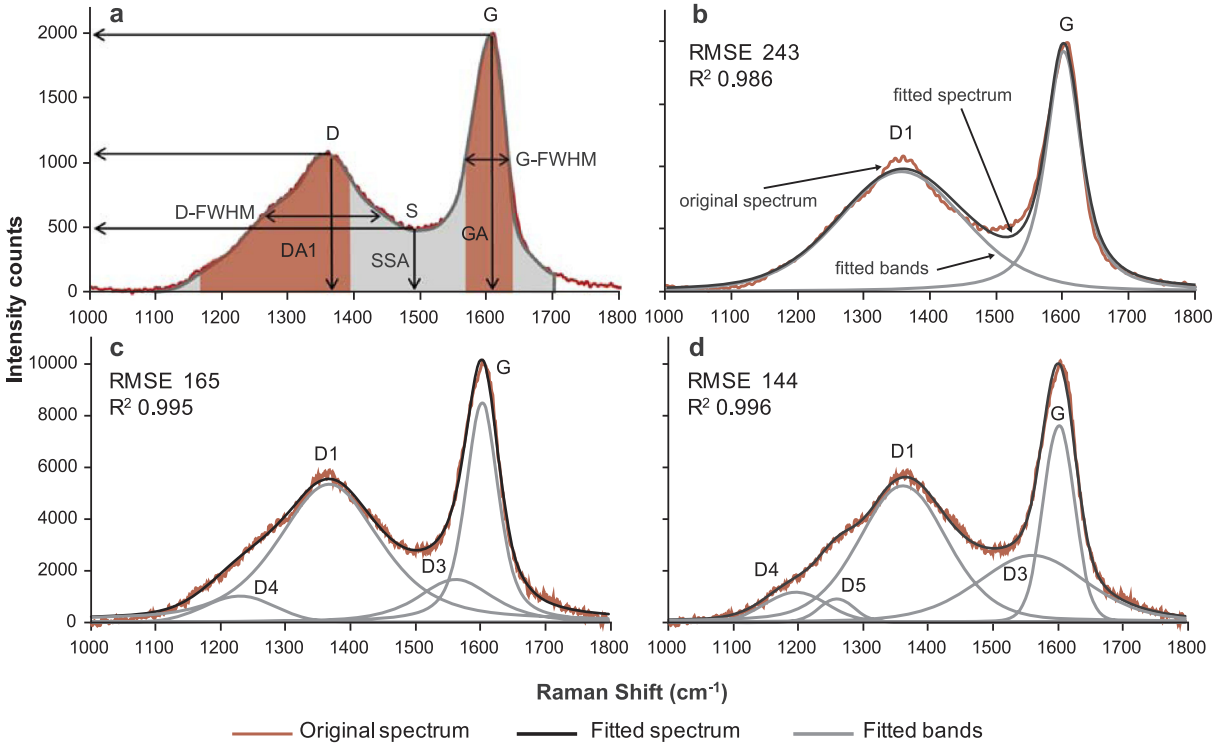

Fig. 11. Comparison of the methods used in this study to determine the Raman features and bands to derive the Raman parameters (Table 1). (a) M-1 and M-2 methods. Deconvolution is not performed. (b) M-3 method. Deconvolution of the G and D1 bands are performed. (c) M-4 method. Deconvolution of the G, D1, D3 and D4 bands are performed. (d) M-5 method. Deconvolution of the G, D1, D3, D4 and D5 bands are performed. Note the RMSE and R^2 values, which statistically show how well the fitted spectrum correlates with the original spectrum, indicate a slightly better fit using method M-5.

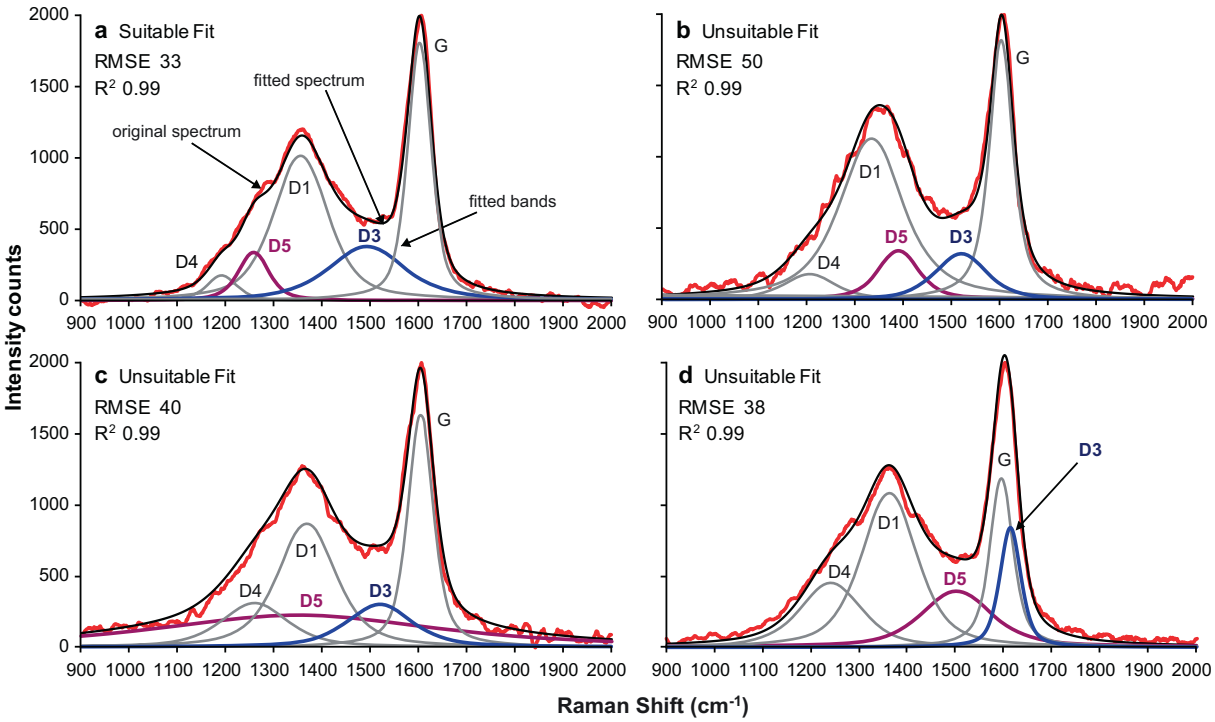

Fig. 12. Common errors associated with deconvolution. Original spectrum is from a phytoclast in sample HC01-04. (a) The curve fitting results are suitable and the bands have reasonable positions, heights and widths. (b) The D5 band has shifted to an unsuitable higher position. (c) The D5 band has moved to an unsuitable position as well as having an unrealistic bandwidth. (d) The D5 and D3 bands have moved to unrealistic positions and the D3 band has an unrealistic height.

whereas the R1 ratio derived from polished blocks has a random distribution with a much larger range. This suggests that during polishing, different particles are affected unequally, as proposed by Ammar and Rouzaud (2012). This crumbling effect during polishing affects the R1 ratio, the saddle index, D-FWHM, DA1/GA and the SSA parameters in a systematic manner. G-FWHM is also affected by polishing but in this case the changes in values are not systematic. The RBS parameter remains largely unaffected.

Sample SSK 4471 is an exception to the general trends, as the results derived from the polished block and strew slide are very similar after

Table 4
Comparison of the results for four Raman parameters derived from methods M-1, M-3, M-4 and M-5 for six samples.

Sample	Method	Parameter							
		R1	RSD (%)	RBS	RSD (%)	G-FWHM	RSD (%)	D-FWHM	RSD (%)
SSK 4522	M-1	0.64	10	240	4	77	8	204	18
	M-3	0.65	14	241	2	77	9	235	6
	M-4	0.61	16	236	4	65	19	128	22
	M-5	0.64	14	236	3	67	16	130	9
SSK 4471	M-1	0.64	5	234	3	83	6	228	9
	M-3	0.63	4	231	2	77	4	241	6
	M-4	0.62	5	229	1	70	5	149	15
	M-5	0.6	7	227	2	70	5	148	20
MPA 61616	M-1	0.61	7	242	4	71	4	215	8
	M-3	0.56	10	243	1	69	7	236	4
	M-4	0.58	10	236	4	62	5	157	9
	M-5	0.55	8	233	2	62	5	138	7
MPA 61619	M-1	0.61	7	246	5	72	7	210	15
	M-3	0.65	19	244	2	68	11	242	14
	M-4	0.57	16	243	4	61	11	137	26
	M-5	0.56	13	244	5	62	10	129	27
HC01-04	M-1	0.61	1	255	4	67	3	209	17
	M-3	0.61	8	249	2	66	8	230	7
	M-4	0.61	14	246	2	56	7	137	12
	M-5	0.61	8	245	2	57	7	128	10
HC02-73	M-1	0.63	9	247	5	67	3	212	13
	M-3	0.63	17	247	2	65	8	206	14
	M-4	0.62	18	242	4	62	10	142	24
	M-5	0.6	18	237	5	61	9	150	27

Mean calculated using a minimum of seven translucent phytoclasts per sample on a strew slide. RSD = relative standard deviation.

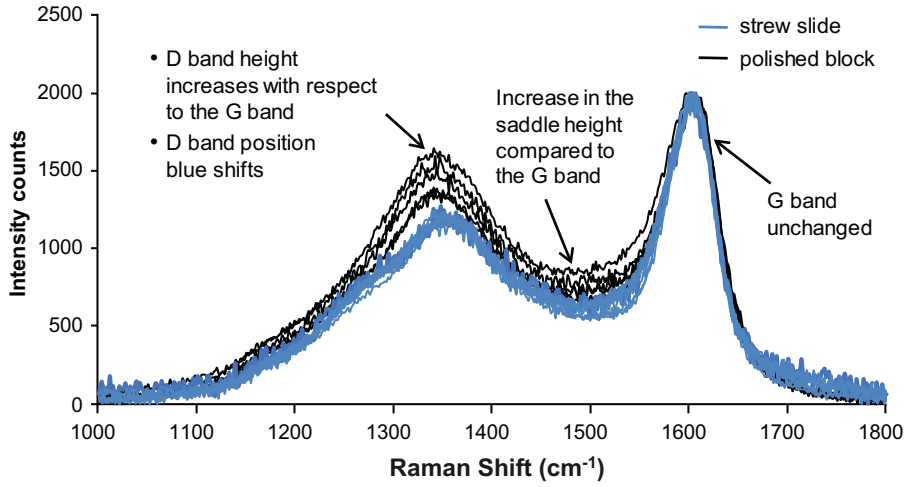

Fig. 13. Comparison of Raman spectra from sample HC01-04 derived from a strew slide and polished block. Only phytoclasts were analysed.

performing a 3rd-order polynomial baseline correction. The reason for this exception is uncertain, but the isolated OM from this sample is composed almost entirely of phytoclasts (Fig. A3.1), whereas the other samples consists predominantly of AOM and some pyrite. One hypothesis is that the varying hardness of the different types of OM and pyrite particles may lead to unequal degrees of polishing and potential heating of individual particles, which may impact the Raman parameters.

Beyssac et al. (2003) and Kouketsu et al. (2014) avoided analyzing the damaged surface of the OM in polished blocks by focusing the laser beam a few micrometres below the surface. This was tested in this study; however, the R1 ratio for several polished blocks did not decrease with depth towards the strew slide sample mean, which suggests that polishing not only impacts the surface, but may also extend below the surface of individual OM particles.

Strew slides exhibit the least amount of bias, as sample preparation does not alter the Raman spectra. In addition, OM types can be easily identified, as well as having the ability to perform conventional standard palynological analysis, spore colouration index (SCI), and other thermal alteration indices (TAI) contemporaneously (cf. Hartkopf–Fröder et al., 2015).

Raman parameters from the opaque phytoclast group (Fig. A3.2) are substantially different compared to the other OM groups. Translucent phytoclast (Fig. A3.1), pseudo-amorphous phytoclast (Fig. A3.2) and AOM (Fig. A3.4) groups have similar Raman parameter values. This is important, as it may be unnecessary to differentiate between these OM types for a rapid assessment of thermal maturity.

Intra-particle variation is apparent in the samples and the results range from 2 to 9%RSD when performing only one measurement on a particle. However, this variation can be reduced to 1–3%RSD, if the average value of 3 measurements is taken from a sample. The intra-particle variation can be attributed to the biogenic heterogeneity. Different thicknesses of the particle may also impact the results, as thinner particles allow the laser to interact with the glass slide, producing greater fluorescence. This could lead to bias in the Raman results if a linear or unsuitable non-linear background correction is performed. Greater fluorescence is also observed close to the edges of the particles and particles with a diameter of $< 3\,\mu m$. It is therefore recommended that thin parts of a particle, as judged by the degree of translucency, small particles of $< 3\,\mu m$, and the edges of particles should be avoided.

The experimental setup affects the OM Raman spectra and parameters. The 514.5 nm Ar-ion laser produces significantly less fluorescence than the 633 nm HeNe laser. Using high laser powers of ≥ 1 mW damages the surface of the OM, which leads to a blue-shift in the G band, the G-FWHM and SSA increases and the D band and saddle heights increase relative to the G band. We recommended a laser power of ~0.2 mW to analyse kerogens, as it does not damage the surface of OM or alter the Raman spectra.

Some previous authors have also used laser powers of < 1 mW (Quirico et al., 2005; Hinrichs et al., 2014; Lünsdorf et al., 2014; Mumm and İnan, 2016; Muirhead et al., 2016; Schito et al., 2017; Schmidt et al., 2017), but the majority of previous studies have employed laser powers > 1 mW (Pasteris and Wopenka, 1991; Spötl et al., 1998; Beyssac et al., 2003; Nestler et al., 2003; Rahl et al., 2005; Schopf et al., 2005; Allwood et al., 2006; Marques et al., 2009; Guedes et al., 2010; Kwiecinska et al., 2010; Lahfid et al., 2010; Liu et al., 2013; Mathew et al., 2013; Kouketsu et al., 2014; Bonoldi et al., 2016; Delarue et al., 2016; Ferralis et al., 2016; Sauerer et al., 2017), which may have induced in-situ thermal damage. JehličKa et al. (2003) and Court et al. (2007) both used laser powers > 1 mW but stated no induced damaged was observed. The reason for this, as mentioned by Court et al. (2007), could be due to the strong noise in the spectra making it difficult to interpret the blue-shift of the G band position. It is also difficult to see the damage if the particle is dark brown/black when analyzing a strew slide.

The Raman instrument set up used in this study showed than an accumulation time of > 10 s does not significantly improve the signal to noise ratio, whereas the number of accumulations, does improve the signal to noise ratio. It is essential that optimum instrumental conditions are developed before conducting Raman analysis. Better quality spectra reduce the bias in picking peak heights and positions when using the M-1 method, and improve reproducibility when performing deconvolution. Some individual OM components generated very noisy spectra and increasing the accumulation time and number of accumulations did very little to improve the signal. These particles were identified as being strongly oxidized (cf. Brolly et al., 2016) and the data acquired were rejected.

Non-linear baseline correction is necessary to analyse low maturity samples, as fluorescence is often present. Linear baseline correction overestimates the R1 parameter, the G-FWHM, the Raman spectra area, and the saddle height, as the linear correction does not take into consideration the curved nature of the background created by the fluorescence. To predict the shape of the background fluorescence, a spectra

Table 5
Mean values and percent relative standard deviation (%RSD) of Raman parameters obtained from strew slides and polished blocks of selected samples.

Sample	Sample type	Statistics	Raman parameter results															
			R1		RBS		RIP		Saddle index		G-FWHM		D-FWHM		DA1/GA		SSA ($\times 10^3$)	
			Linear	3rd-OP	Linear	3rd-OP	Linear	3rd-OP	Linear	3rd-OP	Linear	3rd-OP	Linear	3rd-OP	Linear	3rd-OP	Linear	3rd-OP
SSK 4522	Strew	$\bar{x}$	0.64	0.64	240	240	0.81	0.96	4.13	3.45	79	77	168	204	1.22	1.34	434	457
	slide	%RSD	12	10	4.5	3.8	15	7.3	30	10	9.9	7.8	28	19	28	10	14	6.5
	Polished	$\bar{x}$	0.77	0.69	243	245	1.3	0.91	4.21	4.32	81	79	201	196	1.77	1.55	543	493
	block	%RSD	20	12	5.5	5.1	20	18	28	21	9.3	8.2	28	22	25	15	23	8.3
SSK 4471	Strew	$\bar{x}$	0.64	0.64	235	234	0.94	1.01	3.45	2.46	94	83	222	228	1.25	1.28	398	471
	slide	%RSD	7.5	4.5	3.2	2.9	12	9.8	36	27	10	6	16	9.4	12	8.9	13	8
	Polished	$\bar{x}$	0.71	0.65	233	234	1.17	1.03	2.8	3.7	84	78	214	216	1.47	1.32	534	463
	block	%RSD	12	7.3	4.6	3.9	28	15	37	38	9.8	7.5	17	13	22	10	42	13
MPA 61616	Strew	$\bar{x}$	0.61	0.61	262	242	1.06	1.02	3.85	4.21	74	71	218	215	1.39	1.35	447	424
	slide	%RSD	14	7.1	36	3.9	6.2	4.3	26	7.5	6.5	4.4	12	7.8	11	8.7	5.7	4.6
	Polished	$\bar{x}$	0.79	0.75	249	251	1.6	1	3.22	5.2	71	65	210	189	2.01	1.71	598	454
	block	%RSD	13	15	3.8	3.7	37	17	27	39	12	5.3	22	26	25	51	29	11
MPA 61619	Strew	$\bar{x}$	0.62	0.61	244	246	0.85	0.93	4.2	4.45	75	72	197	210	1.28	1.33	425	411
	slide	%RSD	8.9	6.9	5	5.2	36	14	40	14	6.8	6.7	34	15	23	11	14	10
	Polished	$\bar{x}$	0.78	0.75	255	254	1.03	0.9	2.75	3.1	87	81	211	194	1.68	1.53	532	492
	block	%RSD	12	13	3.4	3.4	6.6	13	9.9	13	8.5	9.1	22	24	11	12	7.2	9
HC01-04	Strew	$\bar{x}$	0.66	0.61	251	255	1.09	1.01	4.25	3.78	69	67	199	209	1.55	1.43	452	428
	slide	%RSD	5.8	1.3	4.8	3.5	16	4.1	26	2.5	11	3.2	15	17	11	1.4	13	1.9
	Polished	$\bar{x}$	0.91	0.94	262	258	1.68	0.84	4.67	4.05	64	60	180	196	1.53	1.82	437	469
	block	%RSD	24	16	4.9	6.3	23	23	28	9.5	21	9.5	26	21	19	15	18	13
HC02-73	Strew	$\bar{x}$	0.63	0.63	257	247	0.97	0.99	4.33	4.9	66	67	196	212	1.39	1.42	417	407
	slide	%RSD	11	8.9	3.9	5.2	11	9.3	17	8.9	3.3	3.3	17	13	14	9.5	6.1	6.1
	Polished	$\bar{x}$	0.77	0.76	248	253	1.45	0.92	2.74	3.16	84	78	204	195	1.8	1.56	604	491
	block	%RSD	12	9	5	6	52	18	24	12	14	8	10	13	22	12	32	7

Note that linear baseline subtraction results in higher RSDs than 3rd-order polynomial baseline subtraction (3rd-OP) and the mean values also differ.

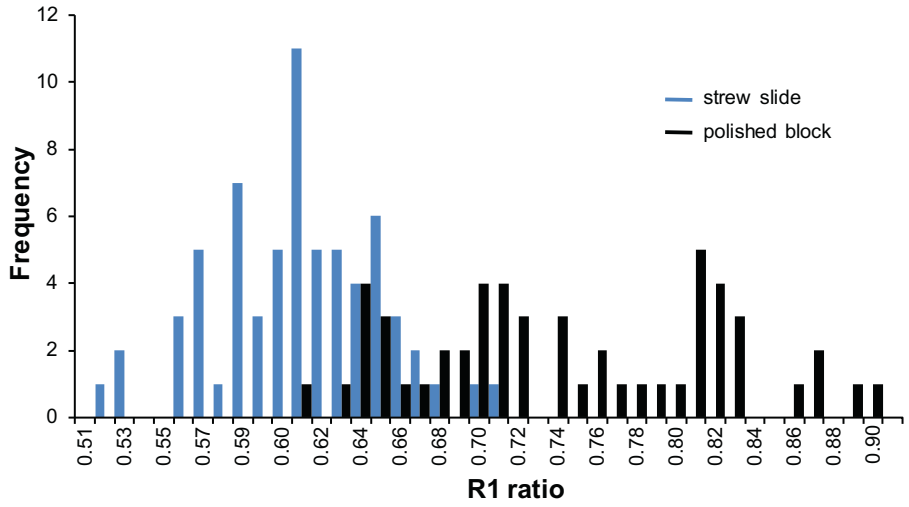

Fig. 14. Comparison of the R1 ratio from sample HC01-04 for a strew slide and a polished block. Note that the polished block produces a greater range and more scattered distribution, whereas the strew samples produces a more normally distributed histogram with less scatter and a smaller range.

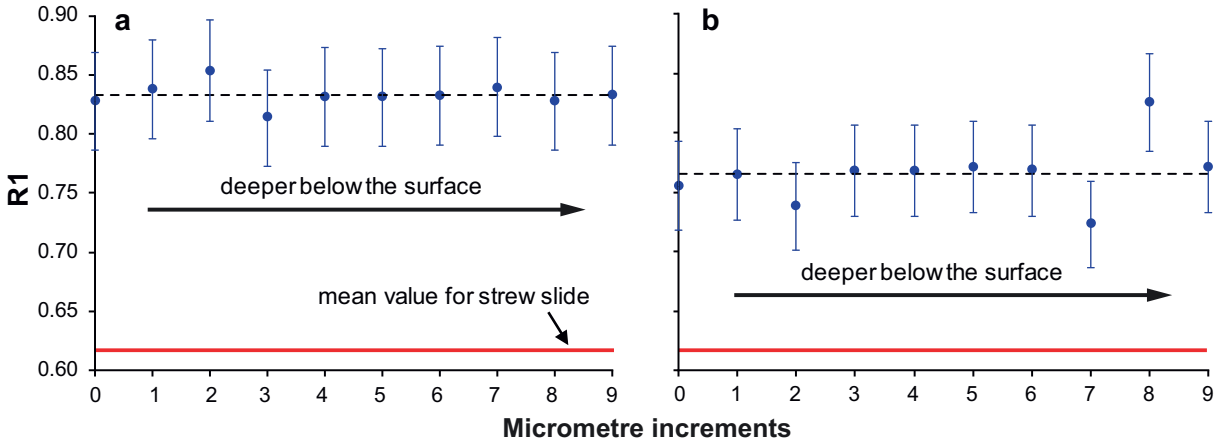

Fig. 15. Depth profile of the R1 ratio derived from two phytoclasts (a) and (b) in a polished block (sample HC01-04), where 0 μm is the surface of the particle.

range of 900–2000 cm^{-1} is proposed in this study.

Five methods were tested in order to calculate Raman parameters, these included: two non-deconvolution methods, the M-1 and M-2 methods; and three deconvolution methods, the M-3, M-4 and M-5 methods. The deconvolution M-3 method has a poorer visual fit with the original spectrum and does not account for the finer detail of the disordered bands between 1200 and 1300 cm^{-1}. The fitted spectra for the M-4 and M-5 methods have a closer fit visually and statistically with the original spectrum. However, this can be misleading, as unrealistic band positions, heights and widths, which are a common problem for the M-4 and M-5 methods, can produce equally good visual and statistical fits.

Kouketsu et al. (2014) avoided the problem of unrealistic band positions in low maturity OM by fixing the position of the D4 band; this method could also be replicated for other bands. This is a more sensible approach than assigning threshold limits, as the experiment is kept consistent. However, this method was not chosen in the present study as the width and heights of the bands are unstable, which results in discrepancies in the other bands. This is a major problem, as a fixed universal deconvolution method applied to low-maturity OM may produce considerable bias.

The M-3 method is simplistic, it ignores the finer detail, and the fitted spectra have a poor resemblance to the original spectrum. On the other hand, the extra bands for the M-4 and M-5 methods have too much freedom of movement, which produces unrealistic band positions, heights and widths. Visual inspection after deconvolution to assess the legitimacy of each band is necessary. A degree of manual tuning is essential. This poses an interesting challenge if an automated deconvolution method is to be developed (Lünsdorf and Lünsdorf, 2016; Lünsdorf et al., 2017).

Nevertheless, deconvolution is heavily used in the literature (Appendix 1), although Kouketsu et al. (2014) and Lünsdorf et al. (2014) acknowledged that there is no agreement on the best way to perform deconvolution for low-maturity OM. Lupoi et al. (2017) also stated that deconvolution is too labour extensive and has inherent bias, which restricts the method as a widespread thermal maturity tool. This study is in agreement with Kouketsu et al. (2014) and Lupoi et al. (2017). We therefore propose that the M-1 and M-2 methods that do not perform deconvolution should be used for low-maturity OM. Both of these methods introduce minimal bias, as well as offering faster data acquisition.

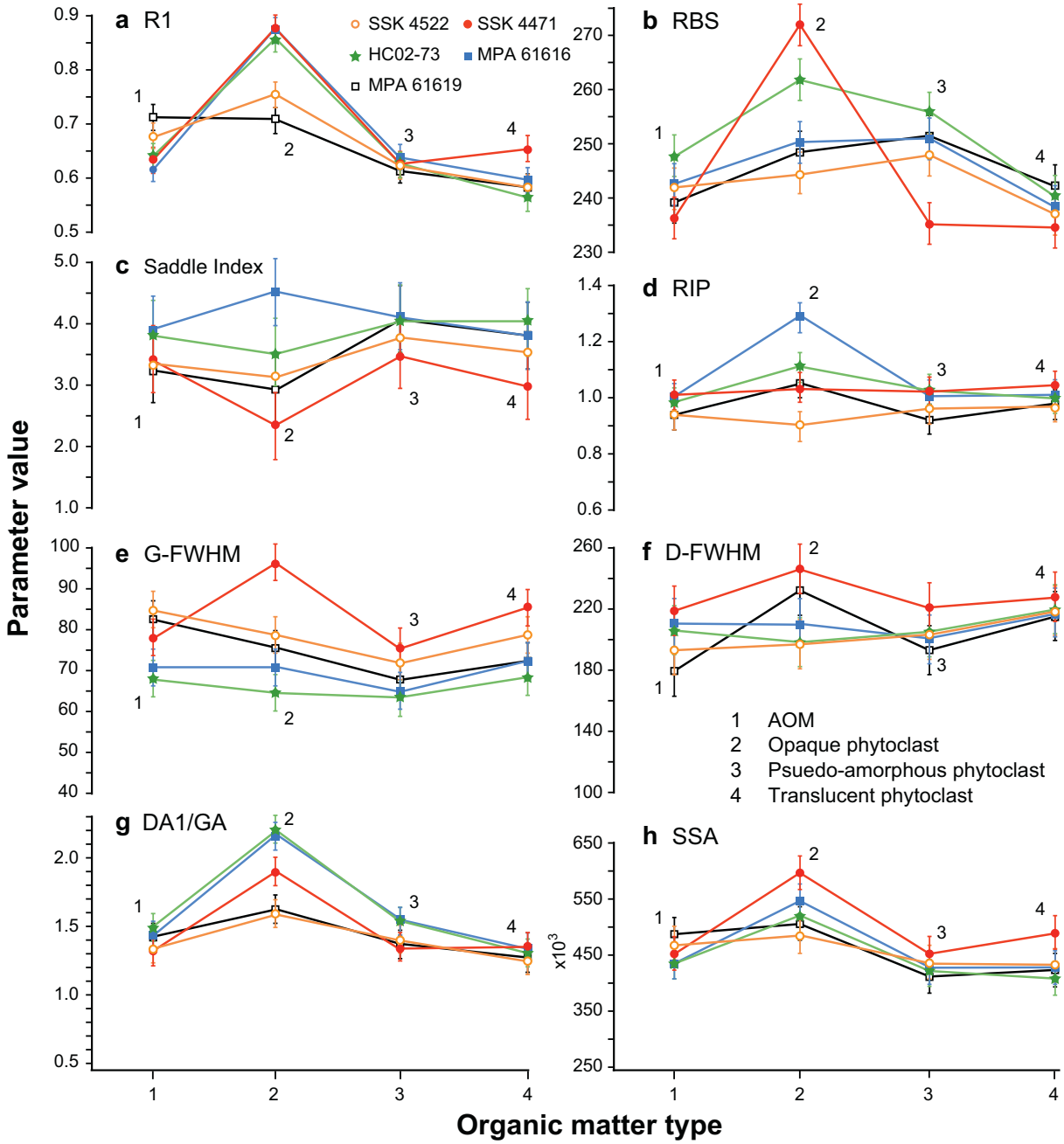

Fig. 16. Raman parameter results of each organic matter type: 1 – AOM; 2 – opaque phytoclast; 3 – pseudo-amorphous phytoclast; 4 – translucent phytoclast (Appendix 3). Data points for each sample are the mean of 7 to 15 measurements and the error bars are 1 sigma standard deviations. (a) R1, (b) RBS, (c) Saddle Index, (d) RIP, (e) G-FWHM, (f) D-FWHM, (g) DA1/DA, (h) SSA.

5. Conclusions

(1) It is recommended that strew slides should be preferred over polished blocks for Raman analysis, which also allow the operator to perform palynofacies analysis and other types of thermal alteration studies (e.g. SCI, TAI) contemporaneously.

(2) The Raman parameters for our low-maturity sample set (0.5–0.8%$_{eq}$VR$_o$) show that there is little difference between the translucent phytoclast, pseudo-amorphous phytoclast and amorphous organic matter groups. However, opaque phytoclasts need to be differentiated. Taking the average value of three measurements across a single particle, as well as avoiding the edges of particles, thin particles and particles with a diameter of < 3 μm, reduce inter-particle variability.

(3) Minimising the noise in the spectra is achieved by using the highest laser power that does not induce damage to the sample. In this study a 514.5 nm laser power of 0.2 mW was used. A better quality spectrum reduces the error associated with selecting the band heights, positions and widths, and makes the baseline correction and deconvolution more reproducible when using an automated method.

(4) A 3rd-order polynomial baseline correction is advised for low-

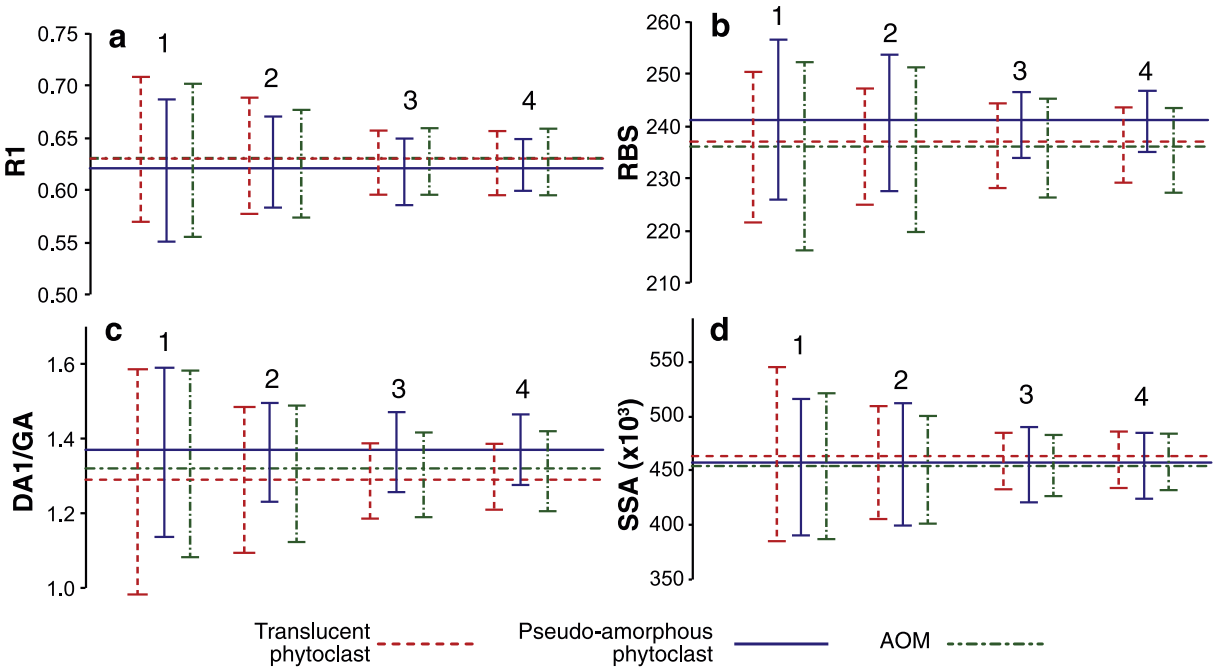

Fig. 17. Intra-sample variation for a translucent phytoclast, pseudo-amorphous phytoclast and AOM in sample SSK 4471. 1: one measurement; 2: average of two measurements; 3: average of three measurements; 4: average of four measurements. The horizontal lines are the average results of 10 single measurements for each particle type. The scatter around the average reduces considerably if an average of ≥3 different measurements across a particle is calculated.

maturity OM. The spectrum needs to be acquired between 900 and 2000 cm^{-1} to predict the non-linearity of the fluorescence.

(5) The reproducibility of using the same deconvolution method across a sample set can be poor and leads to errors. We recommend that deconvolution should not be performed for low-maturity samples. Raman parameters should be acquired using the M-1 and M-2 methods described in this study, which are rapid, robust and require minimal operator manipulation.

Acknowledgements

This work was supported by Kingston University and the University Alliance DTA-Energy programme [grant P1567-100]. Core samples were provided by the British Geological Survey (BGS). Thanks goes to Dr Alastair Baird for his early input in the project. The final manuscript benefitted from the constructive comments of two anonymous reviewers. The International Committee for Coal and Organic Petrology (ICCP) awarded DGH a student travel grant to attend the ICCP course in Potsdam 2017, which played an important role in progressing this study. Outcrop samples were collected as part of a project funded by the Natural Environment Research Council (NERC), Central England Training Alliance (CENTA) consortium [grant NE/L002493/1]. Charlotte Watts is thanked for providing field assistance. We thank the anonymous reviewers for their comments and suggestions to help improve the quality of the paper.

Appendix A. Supplementary data

Supplementary data to this article can be found online at https://doi.org/10.1016/j.coal.2018.03.005.

References

Allwood, A.C., Walter, M.R., Marshall, C.P., 2006. Raman spectroscopy reveals thermal palaeoenvironments of c. 3.5 billion-year-old organic matter. Vib. Spectrosc. 41, 190–197.

Ammar, M.R., Rouzaud, J.N., 2012. How to obtain a reliable structural characterization of polished graphitized carbons by Raman microspectroscopy. J. Raman Spectrosc. 43, 207–211.

Andrews, I.J., 2013. The Carboniferous Bowland Shale Gas Study: Geology and Resource Estimation. British Geological Survey for Department of Energy and Climate Change, London, UK.

Aoya, M., Kouketsu, Y., Endo, S., Shimizu, H., Mizukami, T., Nakamura, D., Wallis, S., 2010. Extending the applicability of the Raman carbonaceous material geothermometer using data from contact metamorphic rocks. J. Metamorph. Geol. 28, 895–914.

Beyssac, O., Goffé, B., Chopin, C., Rouzaud, J.N., 2002. Raman spectra of carbonaceous material in metasediments: a new geothermometer. J. Metamorph. Geol. 20, 859–871.

Beyssac, O., Goffé, B., Petitet, J–.P., Froigneux, E., Moreau, M., Rouzaud, J–.N., 2003. On the characterization of disordered and heterogeneous carbonaceous materials by Raman spectroscopy. Spectrochim. Acta A 59, 2267–2276.

Bonoldi, L., Di Paolo, L., Flego, C., 2016. Vibrational spectroscopy assessment of kerogen maturity in organic-rich source rocks. Vib. Spectrosc. 87, 14–19.

Brolly, C., Parnell, J., Bowden, S., 2016. Raman spectroscopy: caution when interpreting organic carbon from oxidizing environments. Planet. Space Sci. 121, 53–59.

Buseck, P.R., Beyssac, O., 2014. From organic matter to graphite: graphitization. Elements 10, 421–426.

Chen, S., Wu, D., Liu, G., Sun, R., 2017. Raman spectral characteristics of magmatic-contact metamorphic coals from Huainan coalfield, China. Spectrochim. Acta A Mol. Biomol. Spectrosc. 171, 31–39.

Court, R., Sephton, M., Parnell, J., Gilmour, I., 2007. Raman spectroscopy of irradiated organic matter. Geochim.Cosmochim. Acta 71, 2547–2568.

DECC (Department of Energy and Climate Change), 2010. The Unconventional Hydrocarbon Resources of Britain's Onshore Basins – Shale Gas. DECC Promote website, December 2010. https://www.gov.uk/government/uploads/system/uploads/attachment_data/file/367287/Shalegas_uk.pdf.

Delarue, F., Rouzaud, J.-N., Derenne, S., Bourbin, M., Westall, F., Kremer, B., Sugitani, K., Deldicque, D., Robert, F., 2016. The Raman-derived carbonization continuum: a tool to select the best preserved molecular structures in Archean kerogens. Astrobiology 16, 407–417.

Deldicque, D., Rouzaud, J.N., Velde, B., 2016. A Raman e HRTEM study of the carbonization of wood: a new Raman-based paleothermometer dedicated to archaeometry. Carbon 102, 319–329.

Delebarre, J., Ares, E., Smith, L., 2017. Shale Gas and Fracking. vol. 6073 House of Commons Briefing Paper (13 April 2017).

Du, J., Geng, A., Liao, Z., Cheng, B., 2014. Potential Raman parameters to assess the thermal evolution of kerogens from different pyrolysis experiments. J. Anal. Appl. Pyrolysis 107, 242–249.

Emmings, J., Davies, S.J., Vane, C.H., Leng, M.J., Moss-Hayes, V., Stephenson, M.H., Jenkin, G.R.T., 2017. Stream and slope weathering effects on organic-rich mudstone geochemistry and implications for hydrocarbon source rock assessment: a Bowland Shale case study. Chem. Geol. 471, 74–91.

Ferralis, N., Matys, E.D., Knoll, A.H., Hallmann, C., Summons, R.E., 2016. Rapid, direct and non-destructive assessment of fossil organic matter via micro-Raman spectroscopy. Carbon 108, 440–449.

Guedes, A., Valentim, B., Prieto, A.C., Rodrigues, S., Noronha, F., 2010. Micro-Raman spectroscopy of collotelinite, fusinite and macrinite. Int. J. Coal Geol. 83, 415–422.
Hartkopf–Fröder, C., Königshof, P., Littke, R., Schwarzbauer, J., 2015. Optical thermal maturity parameters and organic geochemical alteration at low grade diagenesis to anchimetamorphism: a review. Int. J. Coal Geol. 150–151, 74–119.
Hennissen, J.A.I., Hough, E., Vane, C.H., Leng, M.J., Kemp, S.J., Stephenson, M.H., 2017. The prospectivity of a potential shale gas play: an example from the southern Pennine Basin (central England, UK). Mar. Pet. Geol. 86, 1047–1066.
Hinrichs, R., Brown, M.T., Vasconcellos, M.A.Z., Abrashev, M.V., Kalkreuth, W., 2014. Simple procedure for an estimation of the coal rank using micro-Raman spectroscopy. Int. J. Coal Geol. 136, 52–58.
İnan, I., Goodarzi, F., Schmidt, A., Arouri, K., Qathami, S., Ardakani, O.H., İnan, T., Tuwailib, A.A., 2016. The Silurian Qusaiba Hot Shales of Saudi Arabia: an integrated assessment of thermal maturity. Inter J. Coal Geol. 159, 107–119.
Jarvie, D.M., Claxton, B.L., Henk, G., Breyer, J.T., 2001. Oil and Shale Gas From the Barnett Shale, Fort Worth basin. vol. 85. AAPG National Convention, AAPG Bull, Texas, pp. A100.
JehličKa, J., Urban, O., Pokorný, J., 2003. Raman spectroscopy of carbon and solid bitumens in sedimentary and metamorphic rocks. Spectrochim. Acta A Mol. Biomol. Spectrosc. 59, 2341–2352.
Kelemen, S.R., Fang, H.L., 2001. Maturity trends in Raman spectra from kerogen and coal. Energy Fuel 20, 653–658.
Könitzer, S.F., Davies, S.J., Stephenson, M.H., Leng, M.J., 2014. Depositional controls on mudstone lithofacies in a basinal setting—implications for the delivery of sedimentary organic matter. J. Sed. Res. 84, 198–214.
Könitzer, S.F., Stephenson, M.H., Davies, S.J., Vane, C.H., Leng, M.J., 2016. Significance of sedimentary organic matter input for shale gas generation potential of Mississippian Mudstones, Widmerpool Gulf, UK. Rev. Palaeobot. Palynol. 224, 146–168.
Kouketsu, Y., Mizukami, T., Mori, H., Endo, S., Aoya, M., Hara, H., Nakamura, D., Wallis, S., 2014. A new approach to develop the Raman carbonaceous material geothermometer for low grade metamorphism using peak width. Island Arc 23, 33–50.
Kwiecinska, B., Suárez-Ruiz, I., Paluszkiewicz, C., Rodriques, S., 2010. Raman spectroscopy of selected carbonaceous samples. Int. J. Coal Geol. 84, 206–212.
Lahfid, A., Beyssac, O., Deville, E., Negro, F., Chopin, C., Goffé, B., 2010. Evolution of the Raman spectrum of carbonaceous material in low-grade metasediments of the Glarus Alps (Switzerland). Terra Nova 22, 354–360.
Li, X., Hayashi, J.-I., Li, C.-Z., 2006. FT-Raman spectroscopic study of the evolution of char structure during the pyrolysis of a Victorian brown coal. Fuel 85, 1700–1707.
Liu, D., Xiao, X., Tian, H., Min, Y., Zhou, Q., Cheng, P., Shen, J., 2013. Sample maturation calculated using Raman spectroscopic parameters for solid organics: methodology and geological applications. Chin. Sci. Bull. 58, 1285–1298.
Lünsdorf, N.K., 2016. Raman spectroscopy of dispersed vitrinite - methodical aspects and correlation with reflectance. Int. J. Coal Geol. 153, 75–86.
Lünsdorf, N.K., Lünsdorf, J.O., 2016. Evaluating Raman spectra of carbonaceous matter by automated, iterative curve-fitting. Int. J. Coal Geol. 160–161, 51–62.
Lünsdorf, N.K., Dunkl, I., Schmidt, B.C., Rantitsch, G., von Eynatten, H., 2014. Towards a higher comparability of geothermometric data obtained by Raman spectroscopy of carbonaceous material. Part I: evaluation of biasing factors. Geostand. Geoanal. Res. 38, 73–94.
Lünsdorf, N.K., Dunkl, I., Schmidt, B.C., Rantitsch, G., von Eynatten, H., 2017. Towards a higher comparability of geothermometric data obtained by Raman spectroscopy of carbonaceous material. Part 2: a revised Geothermometer. Geostand. Geoanal. Res. 41, 593–612.
Lupoi, J.S., Fritz, L.P., Parris, T.M., Hackley, P.C., Solotky, L., Eble, C.F., Schlaegle, S., 2017. Assessment of thermal maturity trends in Devonian-Mississippian source rocks using Raman spectroscopy: limitations of peak-fitting method. Front. Energy Res. 5, 24.
Marques, M., Suárez-Ruiz, I., Flores, D., Guedes, A., Rodrigues, S., 2009. Correlation between optical, chemical and micro-structural parameters of high-rank coals and graphite. Int. J. Coal Geol. 77, 377–382.
Marshall, C., Javaux, E., Knoll, A., Walter, M., 2005. Combined micro-Fourier transform infrared (FTIR) spectroscopy and micro-Raman spectroscopy of Proterozoic acritarchs: a new approach to Palaeobiology. Precambrian Res. 138, 208–224.
Mathew, G., De Sarker, S., Pande, K., Dutta, S., Ali, S., Rai, A., Netrawali, S., 2013. Thermal metamorphism of the Arunachal Himalaya, India: Raman thermometry and thermochronological constraints on the tectono-thermal evolution. Int. J. Earth Sci. 102, 1911–1936.
Mcneil, D.H., Schulze, H.G., Matys, E., Bosak, T., 2015. Raman spectroscopic analysis of carbonaceous matter and silica in the test walls of recent and fossil agglutinated foraminifera. AAPG Bull. 99, 1081–1097.
Muirhead, D.K., Parnell, J., Taylor, C., Bowden, S.A., 2012. A kinetic model for the thermal evolution of sedimentary and meteoritic organic carbon using Raman spectroscopy. J. Anal. Appl. Pyrolysis 96, 153–161.
Muirhead, D.K., Parnell, J., Spinks, S., Bowden, S.A., 2016. Characterization of organic matter in the Torridonian using Raman spectroscopy. In: Brasier, A.T., Mcilroy, D., Mcloughlin, N. (Eds.), Earth System Evolution and Early Life: A Celebration of the Work of Martin Brasier. vol. 448. Geol. Soc. London Spec. Publ, pp. 71–80.
Mumm, A.S., İnan, S., 2016. Microscale organic maturity determination of graptolites using Raman spectroscopy. Int. J. Coal Geol. 162, 96–107.
Nestler, K., Dagmar, D., Witke, K., Rößlerc, R., Marx, G., 2003. Thermogravimetric and Raman spectroscopic investigations on different coals in comparison to dispersed anthracite found in permineralized tree fern *Psaronius* sp. J. Mol. Struct. 661–662, 357–362.
Pasteris, J.D., Wopenka, B., 1991. Raman spectra of graphite as indicators of degree of metamorphism. Can. Mineral. 29, 1–9.
Quirico, E., Rouzaud, J., Bonal, L., Montagnac, G., 2005. Maturation grade of coals as revealed by Raman spectroscopy: progress and problems. Spectrochim. Acta A Mol. Biomol. Spectrosc. 61, 2368–2377.
Rahl, J.M., Anderson, K.M., Brandon, M., Fassoulas, C., 2005. Raman spectroscopic carbonaceous material thermometry of low-grade metamorphic rocks: calibration and application to tectonic exhumation in Crete, Greece. Earth Planet. Sci. Lett. 240, 339–354.
Rantitsch, G., Grogger, W., Teichert, C., Ebner, F., Hofer, C., Maurer, E.-M., Schaffer, B., Toth, M., 2004. Conversion of carbonaceous material to graphite within the Greywacke Zone of the eastern Alps. Int. J. Earth Sci. 93, 959–973.
Roberts, S., Tricker, P.M., Marshall, J.E.A., 1995. Raman spectroscopy of chitinozoans as a maturation indicator. Org. Geochem. 23, 223–228.
Sauerer, B., Craddock, P.R., Aljohani, M.D., Alsamadony, K.L., Abdallah, W., 2017. Fast and accurate shale maturity determination by Raman spectroscopy measurement with minimal sample preparation. Int. J. Coal Geol. 173, 150–157.
Savitzky, A., Golay, M.J.E., 1964. Smoothing and differentiation of data by simplified least squares procedures. Anal. Chem. 36, 1627–1639.
Schito, A., Romano, C., Corrado, S., Grigo, D., Poe, B., 2017. Diagenetic thermal evolution of organic matter by Raman spectroscopy. Org. Geochem. 106, 57–67.
Schmidt, J.L., Hinrichs, R., Araujo, C.V., 2017. Maturity estimation of phytoclasts in strew mounts by micro-Raman spectroscopy. Int. J. Coal Geol. 173, 1–8.
Schopf, J.W., Kudryavtsev, A.B., Agresti, D.G., Czaja, A.D., Wdowiak, T.J., 2005. Raman imagery: a new approach to assess the geochemical maturity and biogenicity of permineralized Precambrian fossils. Astrobiology 5, 333–371.
Smith, N.J.P., Turner, P., Williams, G., 2010. UK data and analysis for shale gas prospectivity. In: Vining, B.A., Pickering, S.C. (Eds.), From Mature Basins to New Frontiers. Geol. Soc. London, Proc. 7th Petrol. Geol. Conf.pp. 1087–1098.
Spötl, C., Houseknecht, D.W., Jaques, R.C., 1998. Kerogen maturation and incipient graphitization of hydrocarbon source rocks in the Arkoma Basin, Oklahoma and Arkansas: a combined petrographic and Raman spectrometric study. Org. Geochem. 28, 535–542.
Stephenson, M., 2014. Shale gas activities in Britain: results of a BGS-DECC study on the Bowland and Hodder shales in the North of England. In: Hübner, A., Vetter, A., Horsfield, B. (Eds.), Shale Gas: Factual Scientific Argument For and Against. GFZ German Research Centre for Geosciences.
Tissot, B., Durand, B., Espitalié, J., Combaz, A., 1974. Influence of nature and diagenesis of organic matter in formation of petroleum. AAPG Bull. 58, 499–506.
Tyson, R., 1995. Sedimentary Organic Matter: Organic Facies and Palynofacies. Chapman and Hall, London (615 p).
Waters, C.N., Waters, R.A., Barclay, W.J., Davies, J.R., 2009. A lithostratigraphic framework for Carboniferous successions of southern Great Britain (onshore). In: British Geological Survey, Research Report, (RR/09/01).
Wilkins, R.W.T., Boudou, R., Sherwood, N., Xiao, X., 2014. Thermal maturity evaluation from inertinites by Raman spectroscopy: the 'RaMM' technique. Int. J. Coal Geol. 128, 143–152.
Wilkins, R.W.T., Wang, M., Gan, H., Li, Z., 2015. A RaMM study of thermal maturity of dispersed organic matter in marine source rocks. Int. J. Coal Geol. 150–151, 252–264.
Zeng, Y., Wu, C., 2007. Raman and infrared spectroscopic study of kerogen treated at elevated temperatures and pressures. Fuel 86, 1192–1200.
Zhou, Q., Xiao, X., Pan, L., Tian, H., 2014. The relationship between micro-Raman spectral parameters and reflectance of solid bitumen. Int. J. Coal Geol. 121, 19–25.